

**POLITECNICO DI TORINO**

**Master of Science's Degree in Aerospace Engineering**



**Master Thesis**

**Design of Robust Control Techniques for  
a Small Satellite with Flexible  
Appendages**

**Supervisor**

**Dr. Elisa CAPELLO**

**Candidate**

**Guido BEDIN**

**July 2020**



*To my grandfather Eridiano,  
model of peace and kindness.*

## Abstract

In the latest years, small satellites are becoming more and more utilised by space agencies, thanks to their reduced costs. The technological improvement and the large choice of Components of the Shelf, allowed the space industry to develop smaller and cheaper satellites, able to operate in different missions and scenarios. Due to their limited mass and volume, they can be launched simultaneously with only one launcher, cutting enormously the launch costs. They can be disposed as a constellation and provide services for communications, Earth observation, science experiments or debris removal. All these aspects allowed the non-governmental companies and universities to have access to the space, improving the research of reliable and increasingly smaller satellites, like CubeSats.

Another important characteristic of these satellites is the presence of deployable appendages, like solar arrays, space manipulators, antennas or debris capture systems, to perform different missions and reduce the launch volume. Recent works are focusing the space sector attention to the expandable and inflatable structure, based on flexible materials, in order to cut even more the spacecrafts mass. But small dimensions involve a higher sensibility to external disturbances. Besides, the coupling between the main body of the satellite and the flexible appendages could origin relative oscillations, making the attitude control really hard. Therefore, the attitude control system needs to be robust and reliable enough to dampen the oscillations and maintain the desired attitude.

The aim of this work is to design an attitude control systems, based only on the use of reaction wheels as actuators. In order to do so, a small satellite with two flexible appendages is modelled and two different control techniques are considered: a Linear Quadratic Regulator and a Sliding Mode Control. Eventually, the control system is tested in different mission scenarios.

# Acknowledgements

Beginning from the formal acknowledgments, I would like to thank Dr. Elisa Capello for her patience and knowledge. You taught me a lot, and I honestly think these skills would really help me in my future. I know that I am not the best candidate you ever had, and that you spent a lot of time for me, but I think it was worth it. This thesis is the result of our work.

Now that I can speak informally, I have to thank my parents, for giving me the opportunity to attend the university, my brother Luca for the role play digressions, and the Bingo's sister for these last months of study together. I want also to thank my entire family, from the first uncle to the last cousin. Next Christmas you will not have to ask me how many exams left.

Speaking of friends, there are so many people that helped me throughout these years, that I lost the count. You are so special, I cannot say how grateful I am to be surrounded by such good friends.

A special mention for my little big man Ruggi, you have been like a lighthouse in the dark.

That's all folks, thanks again for everything, I am finally free.



# Table of Contents

<b>List of Tables</b>	v
<b>List of Figures</b>	vi
<b>1 Introduction</b>	1
1.1 The advent of small satellites . . . . .	1
1.2 The debris problem . . . . .	3
1.3 Thesis overview . . . . .	5
<b>2 Base Satellite Model</b>	8
2.1 Reference frames . . . . .	8
2.2 Position equations . . . . .	10
2.3 Attitude equations . . . . .	11
2.3.1 Kinematics . . . . .	11
2.3.2 Dynamics . . . . .	13
2.4 Actuators . . . . .	14
2.4.1 Reaction wheels . . . . .	14
2.4.2 Propulsion system . . . . .	16
<b>3 Flexible Appendages Model</b>	18
3.1 Mathematical model of a flexible satellite . . . . .	18
3.2 External forces applied . . . . .	21
<b>4 Control Laws</b>	23
4.1 Mathematical model of the linearised system . . . . .	24
4.1.1 Linearisation of position equations . . . . .	25
4.1.2 Linearisation of attitude equations . . . . .	26
4.2 Linear Quadratic Control . . . . .	27
4.3 Sliding Mode Control . . . . .	28
4.3.1 First Order SMC . . . . .	30
4.3.2 Continuous Twisting SMC . . . . .	32

<b>5</b>	<b>Simulations Results and Mission Scenarios</b>	<b>34</b>
5.1	Case study . . . . .	34
5.1.1	Simulation of the linear system . . . . .	36
5.2	Comparison between control laws . . . . .	38
5.2.1	CT-SMC . . . . .	45
5.3	Crab Nebula observation mission . . . . .	47
5.4	Debris observation and capture mission . . . . .	51
5.4.1	Observation phase . . . . .	51
5.4.2	Capture phase . . . . .	55
<b>6</b>	<b>Conclusions and Future Works</b>	<b>59</b>
	<b>Bibliography</b>	<b>61</b>

# List of Tables

2.1	RWs parameters [24]	16
2.2	Distribution of forces along the body axes	17
2.3	Characteristics of the 20N chemical monopropellant thruster [25]	17
3.1	Parameters of the Flexible Dynamics	20
3.2	Satellite's dimensions in stowed and deployed conditions	21
4.1	Proposed control gains $k$ [21]	33
4.2	Precision coefficient $\mu$ [21]	33
5.1	Satellite's dimensions	35

# List of Figures

1.1	Debris clouds of the <i>Iridium 33</i> and <i>Cosmos 2251</i> collision [10]	4
1.2	Debris evolution during the years [12]	5
1.3	Artist's view of the MicroSCOPE satellite (credit to CNES)	6
2.1	Graphic representation of different reference frames [14]	9
2.2	Radial boost manoeuvre [13]	11
2.3	RWs in pyramidal configuration [23]	15
2.4	Disposition of the thrusters	16
3.1	Solar arrays deployment	19
3.2	Solar arrays' deployment mechanism [17]	20
4.1	Closed-loop block diagram	23
4.2	Graphic concept of the SMC	28
4.3	Sliding and reaching phases of the SMC. Credit to Liam Vile	29
4.4	Effect of parameter $\lambda$ on $\tanh(\lambda\sigma)$ function	31
4.5	Euler's angles error in time	31
4.6	Control torques of one reaction wheels	32
5.1	Graphic presentation of the solar arrays deployment	35
5.2	Linear system - Angular velocities in time with LQR	36
5.3	Linear system - Euler's angles and error in time with LQR	37
5.4	Comparison of quaternions in time	38
5.5	Comparison of quaternion error in time	39
5.6	Comparison of angular velocities in time	40
5.7	Comparison of control torques in time	41
5.8	Comparison of modal variables in time	42
5.9	1st-SMC - Quaternions in time	43
5.10	1st-SMC - Angular velocities in time	44
5.11	1st-SMC - Modal variables in time	44
5.12	CT-SMC - Quaternions in time	45
5.13	CT-SMC - Quaternion error in time	46

5.14	CT-SMC - Control torques in time . . . . .	46
5.15	Crab Nebula mission - Quaternions in time . . . . .	48
5.16	Crab Nebula mission - Quaternion error in time . . . . .	48
5.17	Crab Nebula mission - Angular velocities in time . . . . .	49
5.18	Crab Nebula mission - Euler's angles in time . . . . .	49
5.19	Crab Nebula mission - Control torques in time . . . . .	50
5.20	Crab Nebula mission - Modal variables in time . . . . .	50
5.21	Observation phase - Quaternion error in time . . . . .	52
5.22	Observation phase - Evolution of position in time . . . . .	52
5.23	Observation phase - Evolution of velocity in time . . . . .	53
5.24	Observation phase - Modal variables in time . . . . .	53
5.25	Observation phase - Control torques in time . . . . .	54
5.26	Observation phase - Control thrusts in time . . . . .	54
5.27	Capture phase - Quaternion error in time . . . . .	56
5.28	Capture phase - Evolution of position in time . . . . .	56
5.29	Capture phase - Evolution of velocity in time . . . . .	57
5.30	Capture phase - Modal variables in time . . . . .	57
5.31	Capture phase - Control torques in time . . . . .	58
5.32	Capture phase - Control thrusts in time . . . . .	58



# Chapter 1

## Introduction

*We choose to go to the Moon. We choose to go to the Moon in this decade and do the other things, not because they are easy, but because they are hard; because that goal will serve to organize and measure the best of our energies and skills, because that challenge is one that we are willing to accept, one we are unwilling to postpone, and one we intend to win, and the others, too.*

With these words J.F. Kennedy announced the decision to achieve one of the most challenging expedition for the mankind, at Rice University of Texas, on September 12th 1962. His speech enlightened maybe the most important peculiarity of humankind: the research of challenges. It is in the human nature to evolve, to travel, to explore, to go beyond the edge of known, because the thirst for knowledge will never be satisfied. All these characteristics have always contribute to the society progress and need to be stimulated in a peaceful way. The days of Cold War are far in the past, there is no more a winner or a loser of the space race, no more difference between nations, now it is up to the men and women of planet Earth to be part of the progress.

### 1.1 The advent of small satellites

Since the launch of the *Sputnik 1*, on October 4th 1957, the space seemed a dangerous environment, accessible only for government agencies, which had large capital to invest and lots of employers and researchers. Years after years, the launchers development allowed the space agencies to launch bigger and heavier spacecrafts, crucial to achieve goals as the Moon landing, the space stations, the rovers on Mars and the probes beyond the edge of the Solar System.

Nevertheless, in recent years, the trend is reversing, and the focus is moving on the small satellites market. Even if in the decade 2009-2018 the average number of small satellite launched per year was 147, it is predicted that this number will

increasing up to 859 in 2019-2028. These numbers imply a big growth in the small satellites market, from 12.6 billion of US dollars in the last decade to 42.6 billion in the next one [9].

There are different reasons that caused these new trend, mainly linked to the launch costs cutting. Small satellites have a mass lower than 500 kg, can be carried simultaneously by a launcher, are composed by lots of COTS<sup>1</sup> and can be used for different missions individually or in constellations. Small satellites are cheap, they require a restricted team to be designed and produced, allowing the non-governmental companies to give their contribution in this sector. It is not surprising, in fact, that the demand for the small satellites industry comes mainly from private agencies, star-up, universities and research centers.

During their lifetime, small satellites need to hold a precise attitude depending on their mission, but they are more sensible to external disturbances and perturbations than large satellites, due to their reduced mass and volume. Besides, if the satellite has some flexible appendages e.g. solar arrays, antennas, space manipulators or others, the attitude control becomes more difficult owing to the oscillations caused by the coupling between the flexible and the rigid parts.

The Attitude Control System works to control autonomously the attitude dynamics and to counteract the external disturbances. This kind of control can be obtained through passive or active stabilization. Passive stabilization is mainly based on spin stabilization, dampers, or gravity gradient stabilization (e.g. gravity booms), but these techniques do not fit with the mission scenarios studied in chapter 5. Instead, active stabilization uses actuators to exchange the momentum of the spacecraft and therefore its attitude. These devices are called Momentum Exchange Devices, and can be divided into the following categories:

- control moment gyros, which consist of a spinning rotor and some motorized gimbals that can cause a gyroscopic torque tilting the rotor;
- reaction wheels, which are at least three spinning wheels disposed in a precise configuration, that can cause a reaction torque on the spacecraft varying their angular velocity;
- magnetorquers, based on the generation of a magnetic dipole, that interact with the Earth's magnetic field providing a reaction torque;
- thrusters disposed in different directions all around the spacecraft, in order to generate a torque when activated.

---

<sup>1</sup>Components Of The Shelf

Active stabilization needs lots of sensors to constantly know the exact attitude of the spacecraft and its angular velocities, in order to process the information through a controller and compute the torques that MEDs have to apply on the spacecraft. These information, unfortunately, are not always available, and the external disturbances can acquire unknown but bounded values. For these reasons, the controller needs to be robust enough to face modelling uncertainties and to work under sets of non predicted parameters.

This thesis aim to design a robust control system comparing two different techniques: the Linear Quadratic Regulator and the Sliding Mode Control. The LQR has been chosen due to its simplicity and precision when it is used with linear system. Instead, the SMC well respond to uncertainties and perturbations. The two controllers have been tested in different mission scenarios and situations, to better understand the limits of their control capability, and under what conditions the modelled system diverges.

## 1.2 The debris problem

Space always looked like an empty and infinite place where there was no need to be worry about the so call *space junk*. For many years, the space agencies sent lots of spacecrafts on orbit, not thinking about the de-orbiting problem. Launch after launch, the number of boosters, dead satellites and debris orbiting around the Earth has rapidly increased.

In 1991, the astrophysicist and NASA consultant Donald J. Kessler, report to the US space agency his concerning about the space debris. He illustrated a scenario became famous with the term of *Kessler's Syndrome*, where the uncontrolled number of orbital debris could have lead to an augmentation of orbital collisions, releasing a cascade effect that could cause an exponential growth of debris and collisions. In this scenario, the Low Earth Orbit becomes inaccessible and the majority of the actual satellites and constellations destroyed by the debris [7]. It is useless to say that this could be a real catastrophe, with huge consequences on our lives and on the technological development.

This scenario became partially true in February 10th 2009, with the *Iridium 33* and *Cosmos 2251* collision. According to the Debris Analysis Response Team (DART) [11], the impact caused the total destruction of the two satellites, generating over 2200 debris larger than 10 cm and hundreds of thousands too small to be tracked, generating two debris clouds as shown in figure 1.1. The estimations of the DART foresee that it will take 40 to 50 years before all the debris will burn in the atmosphere. This incident had a big impact in terms of costs and space security, in fact, the ISS had to operate a collision avoidance manoeuvre in October 27th 2014, in order to transfer the space station on a safer orbit during the passage of

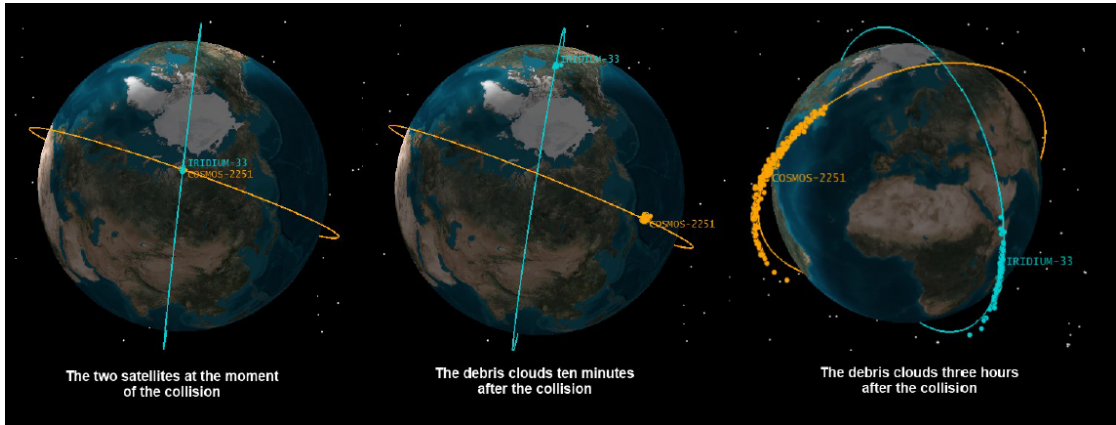


**Figure 1.1:** Debris clouds of the *Iridium 33* and *Cosmos 2251* collision [10]

some of these debris [2].

Other collisions have been detected throughout the years, like the one in 1996 between the French reconnaissance satellite *Cerise* and a debris of an *Ariane* launcher exploded in 1986, or the CubeSat *NEE-01 Pegaso* that collided in 2013 with the upper stage of a *Tsyklon-3* launcher, in orbit since 1985 [3].

The most dangerous aspect of this collision are the debris under the 5 cm of dimension (as said from the Darmstadt Space Debris Office Head, Holger Krag [26]), because they are too small to be located and to keep track of their orbit. Due to the high orbital velocity in the LEO ( $7 \div 8$  km/s [8]), even a small screw could potentially cause serious damage to a satellite or, even worse, to the ISS. *Sentinel-1A* satellite has been victim of one of this ghost debris, in August 23th 2016, when one of its solar arrays has been hit causing a decrease in the electric power generation. Luckily, the mission has not been compromised and the *Sentinel-1A* is still operative.

The external disturbances, like the residual atmospheric drag in LEO and the solar pressure, can help the debris to re-entry in the atmosphere and burn during the fall. However, this process could take years or even decades. Meanwhile, the Earth orbits are becoming overpopulated, as shown in figure 1.2. Thus, it is obvious that the human intervention is required.

In the latest 90's, many space agencies and universities have began to study different technologies and solutions to reduce and remove debris. The Inter-Agency Space Debris Coordination Committee groups many space agencies like NASA, ESA, ROSCOSMOS, ASI and other, to exchange information on space debris research and to observe some guidelines in order to mitigate the problem [4].

The fruits of researchers' effort have been proposed and partially tested, like the ESA e.Deorbit mission [6] and the JAXA KITE mission [5]. These missions consist

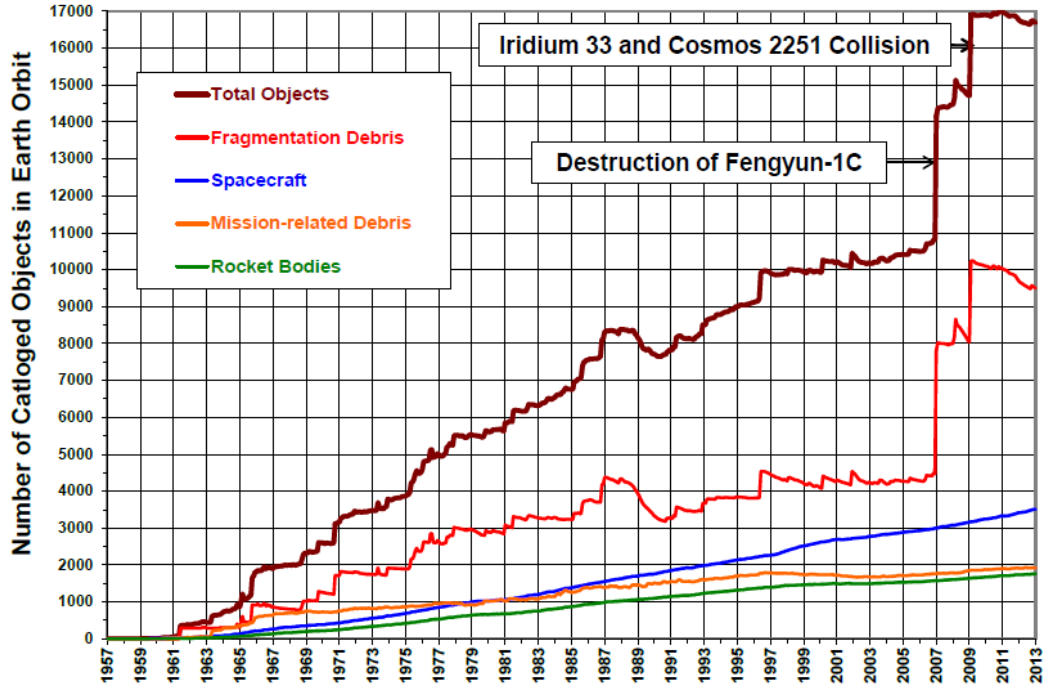


Figure 1.2: Debris evolution during the years [12]

of experimenting capture systems like nets, robotic arms, harpoons and other technologies that require a high level of attitude and position control, in order to catch the target. The worst scenario that could happen is a collision between the chaser and the target, providing more debris, therefore it is crucial to consider how the flexible appendages affect the chaser attitude and how the inertia variation after capture compromises the chaser control capability.

### 1.3 Thesis overview

The principal objective of this thesis is to design a robust attitude controller for a small satellite with flexible appendages, and to demonstrate that a linear controller is not able to guarantee the control, therefore a non linear controller is needed. To do so, the satellite and the appendages have been modelled and different simulations have been run with the use of the software *MATLAB Simulink*. This software is really intuitive to use and easy learning, advisable to visualize the behaviour of non linear system.

The modelled satellite has been inspired to the CNES/ESA MicroSCOPE spacecraft (see figure 1.3), with a mass of 290 kg, dimensions of  $1.38 \times 1.04 \times 1.58$

meters in stowed configuration, two 1 DoF<sup>2</sup> solar arrays, a group of four reaction wheels as actuators and a propulsion system for the position control. The base satellite has been modelled as a rigid body, and the appendages as flexible components.



**Figure 1.3:** Artist's view of the MicroSCOPE satellite (credit to CNES)

To better expose the presented work, this thesis is structured in five different chapters, in addition to the introductory chapter.

In Chapter 2 the base satellite model is presented and some theory recalls are given. The position and attitude dynamics and kinematics are explained with the use of Hill's equation, quaternions and Euler's angle. Secondly, the linear system for position and attitude control is presented, and the characteristics of the actuators implemented are reported.

In Chapter 3 the flexible satellite is modelled, showing to the reader the alterations of the satellite dynamics, due to the coupling between flexible and rigid model. In order to force further the system, a forcing with variable frequency and amplitude is implemented in the last section of the chapter.

Chapter 4 is about laws of control, especially the Linear Quadratic Regulator

---

<sup>2</sup>Degrees of Freedom

(LQR) and the Sliding Mode Control (SMC). These two laws of control are explained in the detail and for the last one are proposed two different regulators: a First Order Sliding Mode Control and a Continuous Twisting Sliding Mode Control.

In Chapter 5 different mission scenarios are analyzed:

- attitude control for the Crab Nebula observation. The satellite has an undefined initial attitude and has to point towards the Crab Nebula, while the solar arrays are deployed. After the manoeuvre, the satellite rotates to point to the ideal quaternion;
- attitude and position control for a debris observation and capture mission. The satellite has to capture a debris, while the solar arrays are deployed. First it rotates to reach the required attitude to observe the target, then it approaches the debris to captures it and eventually returns to the initial attitude.

In the first section the case study is presented (CNES/ESA satellite MicroSCOPE), with all the data and indications useful to run the simulations. The successive sections are about the mission scenarios and simulations run to confront the different control laws.

Eventually, Chapter 6 draws conclusions of this thesis and presents future works that can be done to enlarge this one.

# Chapter 2

## Base Satellite Model

In this chapter the attitude and position of the base satellite is modelled considering the spacecraft as a rigid body. The dynamics and kinematics of the satellite are explained with the Hill's equation of motion and the Euler's parameters, also known as quaternions.

As previously said, the spacecraft considered in this thesis is a small satellite orbiting in a LEO<sup>1</sup> and equipped with reaction wheels and a cold gas propulsion system.

In the first section the reference frames used in this work are presented, in the second one the position dynamics equations are computed and in the third one the mathematical model for the attitude dynamics and kinematics is explained. At last, the modeling of the actuators is exposed.

### 2.1 Reference frames

To study the guidance and control of the satellite, it is important to show the reference frames that are taken into account. In this thesis, three main right-handed frames are considered: an inertial frame, a spacecraft local frame and a body frame.

The inertial frame chosen is the ECI frame (Earth-centered Inertial). This frame has its origin in the center of mass of the Earth, the x-axis is in vernal equinox direction, the z-axis in Earth's rotation direction and the x-y plane lies on the equatorial plane. This frame is not fixed to the Earth and it is non-rotating with respect to the stars, except for the precession of the equinoxes. For this reason, due to the non-uniformity of the gravitational field, the ECI frame is a quasi-inertial frame, but, for the spacecraft in exam and the mission scenario explained in Chapter 5, it can be considered inertial.

---

<sup>1</sup>Low Earth Orbit

The local frame chosen is the LVLH frame. The origin is in the satellite center of mass, the x-axis lies along the direction of orbital motion, the z-axis points towards the Earth's center of mass and the y-axis completes the triad.

Eventually, the body reference frames has its origin in the satellite's center of mass and the axis orientation changes according to the mission scenario. In this work, the body axis have been chosen to be principal axis of inertia, therefore the inertia tensor of the base satellite  $J_{bs}$  is a diagonal matrix:

$$J_{bs} = \begin{bmatrix} J_{xx_b} & 0 & 0 \\ 0 & J_{yy_b} & 0 \\ 0 & 0 & J_{zz_b} \end{bmatrix} \quad (2.1)$$

where  $J_{xx_b}$ ,  $J_{yy_b}$  and  $J_{zz_b}$  are the moments of inertia with respect to the body reference frame.

Figure 2.1 shows the reference frames previously described. The transformation of a vector from one reference frame to another is realized with the rotation-matrices, with the following sequence order: 3 – 2 – 1.

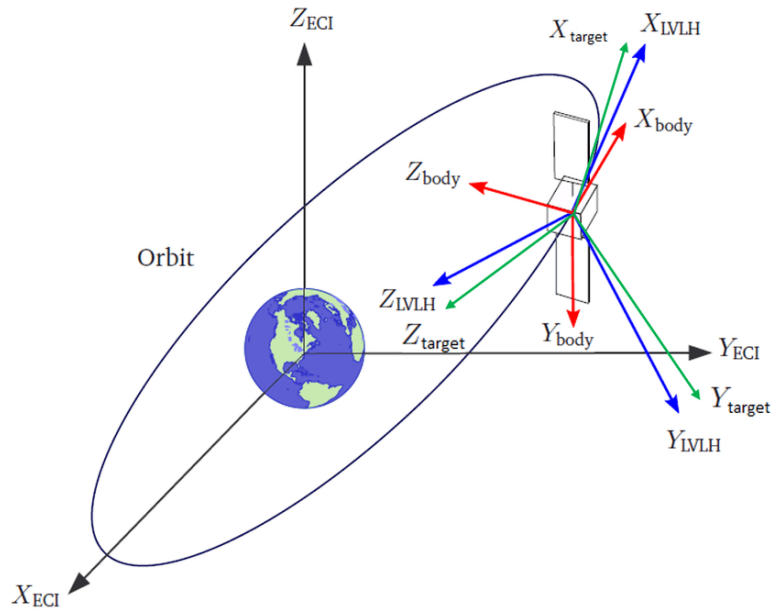


**Figure 2.1:** Graphic representation of different reference frames [14]

## 2.2 Position equations

As previously said in Chapter 1, different mission scenarios are considered in this thesis. In one of this scenario the satellite in exam has to capture a target object, like a debris or a dead satellite. Considering an inertial reference frame (e.g. the ECI frame), let  $\mathbf{r}_c$  be the chaser satellite position vector and  $\mathbf{r}_t$  the target position vector, the relative position and acceleration vectors of the chaser w.r.t. the target can be expressed as:

$$\begin{cases} \mathbf{s} = \mathbf{r}_c - \mathbf{r}_t \\ \ddot{\mathbf{s}} = \ddot{\mathbf{r}}_c - \ddot{\mathbf{r}}_t \end{cases} \quad (2.2)$$

The target spacecraft is subjected only to the Newton's law of gravitation. The chaser, instead, has a cold-gas propulsion system that can produce a variable thrust  $\mathbf{F}$ , therefore its mass  $m_c$  is variable. Hence, the acceleration vectors of the two spacecrafts can be computed.

$$\begin{cases} \ddot{\mathbf{r}}_t = -\mu \frac{\mathbf{r}_t}{r_t^3} \\ \ddot{\mathbf{r}}_c = -\mu \frac{\mathbf{r}_c}{r_c^3} + \frac{\mathbf{F}}{m_c} \end{cases} \quad (2.3)$$

where  $\mu$  is the geocentric gravitational constant ( $\mu = GM_E$ , with  $G$  the universal gravitational constant and  $M_E$  the mass of the Earth).

Substituting equation 2.3 into equation 2.2 and adopting a transformation from ECI to target's LVLH frame, with some passages it is possible to derive the Hill's equation of motion of the two spacecrafts. Considering the orbital rate  $n = \sqrt{\mu/r_t^3}$  as a constant, the equations are the following:

$$\begin{cases} \ddot{x} = \frac{F_x}{m_c} + 2n\dot{z} \\ \ddot{y} = \frac{F_y}{m_c} - n^2y \\ \ddot{z} = \frac{F_z}{m_c} - 2n\dot{x} + 3n^2z \end{cases} \quad (2.4)$$

Note that these equations are valid only for circular orbit and when the distance between the chaser and the target is lower than the orbital radius. Under these hypothesis, the LVLH frame can be considered a quasi-inertial reference frame, therefore, if the chaser's attitude is known, it is possible to evaluate the thrust needed in the body frame to capture the target.

The rendez-vous manoeuvre adopted in this thesis is the radial boost manoeuvre shown in Fig. 2.2, where *V-bar* and *R-bar* are respectively  $x_{LVLH}$  and  $z_{LVLH}$ .

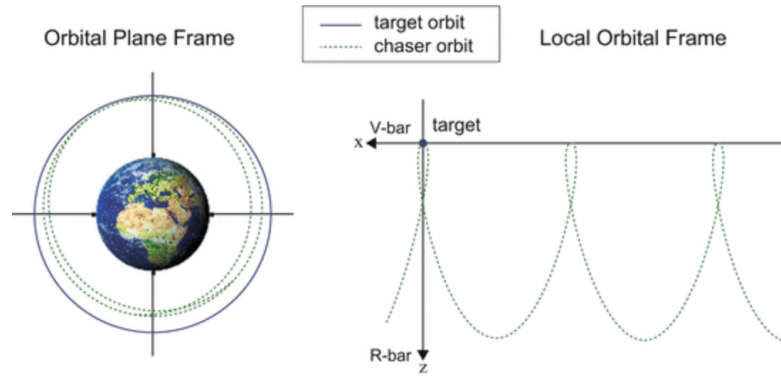


Figure 2.2: Radial boost manoeuvre [13]

## 2.3 Attitude equations

### 2.3.1 Kinematics

The kinematics of the base satellite is studied with the use of quaternions. According to William Rowan Hamilton [1], a quaternion is an algebraic quantity composed by four constituents ( $q_0, q_1, q_2, q_3$ ) and three imaginary quantities ( $i, j, k$ ), that represent an array with one scalar component and a vector with three elements:

$$\mathbf{q} = q_0 + q_1i + q_2j + q_3k \quad (2.5)$$

In this thesis the scalar-first convention is chosen, so the scalar component is the first element of the quaternion,  $q_0$ , and  $q_{123}$  represent the vector part of the quaternion. Quaternions can be used to describe the transformation between two reference frames instead of Euler's angles, using only algebraic operation and avoiding singularities.

According to Euler's theorem: "*The most general motion of a rigid body with one point fixed is a rotation about an axis through that point*". Let  $\nu$  be the axis and  $\alpha$  the rotation over that axis, the quaternion representing the orientation of the rigid body can be computed as follows:

$$q_0 = \cos(\alpha/2) \quad q_{123} = \hat{\nu} \cdot \sin(\alpha/2)$$

where  $\hat{\nu}$  is the unit vector in direction of  $\nu$ .

Quaternions can be easily summed and differenced by summing and differencing the constituents of the quaternions, e.g:

$$\mathbf{q} \pm \mathbf{r} = q_0 \pm r_0 + (q_1 \pm r_1)i + (q_2 \pm r_2)j + (q_3 \pm r_3)k$$

Regarding the product of two quaternions, instead, to reduce it in a quaternion form, the imaginary quantities have to follow the rules reported in equations 2.6:

$$\begin{cases} i^2 = j^2 = k^2 = 1 \\ ij = k & jk = i & ki = j \\ ji = -k & kj = -i & ik = -j \end{cases} \quad (2.6)$$

Thus the product of two quaternions  $q$  and  $r$  is:

$$q \otimes r = \begin{bmatrix} q_0 & -q_1 & -q_2 & -q_3 \\ q_1 & q_0 & -q_3 & q_2 \\ q_2 & q_3 & q_0 & -q_1 \\ q_3 & -q_2 & q_1 & q_0 \end{bmatrix} \cdot \begin{bmatrix} r_0 \\ r_1 \\ r_2 \\ r_3 \end{bmatrix} \quad (2.7)$$

Note that the norm of a quaternion is always equal to the unit:

$$q_0^2 + q_1^2 + q_2^2 + q_3^2 = 1$$

It is now possible to evaluate the evolution of quaternions in time:

$$\dot{q} = \frac{1}{2} O(\omega_B) q \quad (2.8)$$

where  $\omega_B$  is the angular velocities vector in the body reference frame, and  $O(\omega_B)$  is a  $\mathfrak{R}^{4 \times 4}$  matrix:

$$O(\omega_B) = \begin{bmatrix} 0 & -\omega_x & -\omega_y & -\omega_z \\ \omega_x & 0 & -\omega_z & \omega_y \\ \omega_y & \omega_z & 0 & -\omega_x \\ \omega_z & -\omega_y & \omega_x & 0 \end{bmatrix}$$

Equation 2.8 describes the kinematics of the base satellite, bonding together the orientation, with respect to the inertial frame, to the angular velocities. Note that the quaternion error between the measured and desired condition cannot be evaluated as difference of two quaternions, but has to be computed as a quaternion product.

$$q_{err} = q_{des}^{-1} \otimes q_{true} \quad (2.9)$$

Where  $q^{-1}$  is the quaternion inverse:

$$q^{-1} = \frac{[q_0 \ -q_1 \ -q_2 \ -q_3]^T}{norm(q)}$$

It can be useful to express the satellite's attitude with the Euler's angles  $[\phi \ \theta \ \psi]^T$ , to more easily visualize its orientation in space. The transformation from quaternions to Euler's angles can be done as follows:

$$\begin{bmatrix} \phi \\ \theta \\ \psi \end{bmatrix} = \begin{bmatrix} \arctan \frac{2(q_0 q_1 + q_2 q_3)}{q_0^2 + q_1^2 - q_2^2 - q_3^2} \\ \arcsin 2(q_0 q_2 - q_1 q_3) \\ \arctan \frac{2(q_1 q_3 + q_0 q_2)}{q_0^2 - q_1^2 - q_2^2 + q_3^2} \end{bmatrix} \quad (2.10)$$

### 2.3.2 Dynamics

The base satellite's dynamics is based on the study of the angular momentum. The total angular momentum of a rigid body (composed by  $n$  parts) is related to the mass, position and velocity of the body w.r.t. inertial reference frame.

$$\mathbf{H}_{tot} = \sum_{i=1}^n \mathbf{r}_i \times m_i \dot{\mathbf{r}}_i$$

To transpose the angular momentum in a body frame, it has to be decomposed into two addenda: the angular momentum of total mass w.r.t. inertial origin and the body angular momentum about center of mass. Considering  $\mathbf{R}$  as the distance between the inertial frame origin and the body frame origin, the position  $\mathbf{r}_i$  of the  $i^{th}$  mass is given by  $\mathbf{r}_i = \mathbf{R} + \boldsymbol{\rho}_i$ , where  $\boldsymbol{\rho}_i$  is the position of the  $i^{th}$  mass w.r.t. the body frame origin. Therefore the above equation can be written as follows:

$$\mathbf{H}_{tot} = \left( \sum_{i=1}^n m_i \right) \mathbf{R} \times \dot{\mathbf{R}} + \sum_{i=1}^n m_i \boldsymbol{\rho}_i \times \dot{\boldsymbol{\rho}}_i$$

Knowing that the term  $\dot{\boldsymbol{\rho}}_i$  is given by the cross product between  $\boldsymbol{\rho}_i$  and the angular velocity  $\boldsymbol{\omega}$ , the angular momentum can be expressed as  $\mathbf{H}_B = J_B \boldsymbol{\omega}$ , where  $J_B$  is the inertia matrix in the body frame.

If Momentum Exchange Devices are present on the satellite, the total angular momentum has to consider the angular momentum due to the MEDs. As previously said, the satellite in exam is equipped with reaction wheels.

$$\mathbf{H}_{tot} = \mathbf{H}_{sat} + \mathbf{H}_{MED} \quad (2.11)$$

To evaluate the dynamics of the satellite, it is necessary to consider the total torques acting on the rigid body, that can be divided into external and internal torques. The internal torques are the ones generated by the MEDs (the reaction wheels). Instead, the external torques are the ones due to external disturbances, and can be expressed as:

$$\mathbf{T}_{ext} = \frac{d}{dt}(\mathbf{H}_{tot}) = \dot{\mathbf{H}}_{sat} + \dot{\mathbf{H}}_{RW} \quad (2.12)$$

Considering that there are no variations of inertia in time, the derivative of the angular momentum can be written as  $\dot{\mathbf{H}} = J\dot{\boldsymbol{\omega}}$ .

With a transformation from inertia to body frame and with a few passages, the following equations can be deduced.

$$\begin{aligned} \mathbf{T}_{ext} &= J_{bs} \dot{\boldsymbol{\omega}}_B + \boldsymbol{\omega}_B \times J_{bs} \boldsymbol{\omega}_B + \mathbf{u} - \boldsymbol{\omega}_B \times J_{RW} \boldsymbol{\omega}_{RW} \\ \dot{\boldsymbol{\omega}}_B &= J_{bs}^{-1} (\mathbf{T}_{ext} + \mathbf{u} - \boldsymbol{\omega}_B \times (J_{bs} \boldsymbol{\omega}_B + J_{RW} \boldsymbol{\omega}_{RW})) \end{aligned} \quad (2.13)$$

Equation 2.13 is also known as Euler's equation, and represents the dynamics of the base satellite in the body reference frame, where  $\mathbf{u}$  is the control input, i.e. the torque generated by the reaction wheels.

There are different external disturbances affecting the spacecrafts in the Earth's orbits, such as the gravity gradient, solar radiation pressure, atmospheric drag and magnetic torque due to residual dipole. The gravity gradient is the only one taken into account in the term  $T_{ext}$ , because the others are considered negligible in this work.

The gravity gradient torque depends on the satellite inertia matrix and can be expressed as follow:

$$\mathbf{T}_{gg} = \frac{3\mu}{r^3} \hat{\delta}_3 \times (J_{sat} \hat{\delta}_3) \quad (2.14)$$

where  $\hat{\delta}_3$  is the third column of the DCM<sup>2</sup> from body to LVLH frame, according to the rotation sequence 3 – 2 – 1. Considering  $[\phi, \theta, \psi]^T$  as the rotation angles, and indicating  $\cos(\alpha)$  as  $c\alpha$  and  $\sin(\alpha)$  as  $s\alpha$ , the DCM can be written as [15]:

$$DCM = \begin{bmatrix} c\psi c\theta & c\theta s\psi & -s\theta \\ s\phi s\theta c\psi - c\phi s\psi & s\phi s\theta s\psi + c\phi c\psi & s\phi c\theta \\ c\phi s\theta c\psi + s\phi s\psi & c\phi s\theta s\psi - s\phi c\psi & c\phi c\theta \end{bmatrix}$$

In the real world there are also some internal disturbances that can affect the satellite attitude, generated by the actuators, but in this thesis all the spacecraft's components are considered as ideal ones, therefore the internal disturbances are neglected. A further consideration has been made about the flexible appendages, in Chapter 3.

## 2.4 Actuators

As introduced in Section 1.3, the base satellite is equipped with two kind of actuators: a group of four reaction wheels and a cluster of thrusters. In this section, some considerations about these actuators are given, to better understand the attitude and position control system modelled in this thesis.

### 2.4.1 Reaction wheels

Reaction wheels (RWs) are one of the most used actuators for the attitude control, thanks to their reliability and fast response, even if they present the saturation

---

<sup>2</sup>Direction Cosine Matrix

problem. Three reaction wheels are needed to guarantee the control on the satellite's body axes, but usually they are designed in group of four to face possible failures.

In this work, the pyramidal configuration has been adopted, as shown in figure 2.3. Considering a body reference frame local to each RW, with the origin in the RW's center of mass, and the axis  $z_{RW}$  coinciding with the RW's axis of rotation, then the  $\beta$  angle is the skew angle between the  $z_{RW}$  axis and the plane  $x_{body} - y_{body}$  of the base satellite. Hence, each wheel generates angular momentum along its  $z_{RW}$  axis, acting in different direction w.r.t. the base satellite body frame.

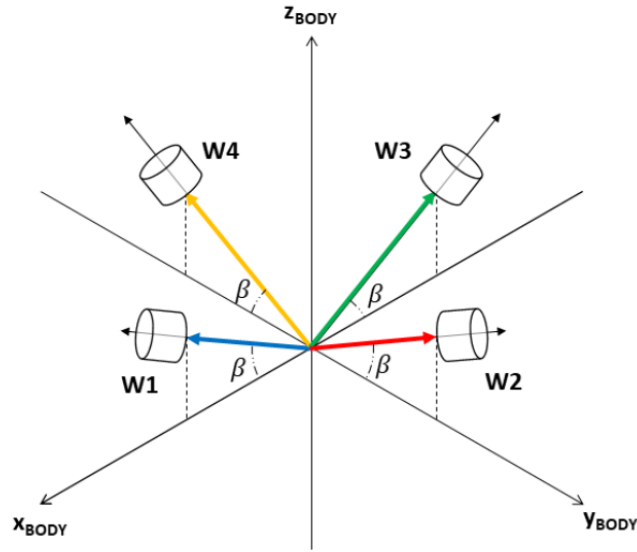


**Figure 2.3:** RWs in pyramidal configuration [23]

In order to understand the momentum and torques generated by the RWs in the satellite body frame, the  $Z$  matrix reported in equation 2.15 is needed.

$$Z = \begin{bmatrix} \cos(\beta) & 0 & -\cos(\beta) & 0 \\ 0 & \cos(\beta) & 0 & -\cos(\beta) \\ \sin(\beta) & \sin(\beta) & \sin(\beta) & \sin(\beta) \end{bmatrix} \quad (2.15)$$

In this work, the reaction wheels chosen are the model  $RW4$  from Blue Canyon Technologies, with the characteristics reported in table 2.1. They are composed of brushless DC motors and ultra-smooth bearing, and they are disposed with a skew angle of  $\beta = 30^\circ$ . Thus the  $Z$  matrix becomes the following:

$$Z = \begin{bmatrix} \frac{\sqrt{3}}{2} & 0 & -\frac{\sqrt{3}}{2} & 0 \\ 0 & \frac{\sqrt{3}}{2} & 0 & -\frac{\sqrt{3}}{2} \\ \frac{1}{2} & \frac{1}{2} & \frac{1}{2} & \frac{1}{2} \end{bmatrix}$$

Momentum	Max torque	Mass	Volume	Power
4.0 Nms	0.25 Nm	3.2 kg	$17 \times 17 \times 7$ cm	$< 10$ W

**Table 2.1:** RWs parameters [24]

## 2.4.2 Propulsion system

There are several kinds of thrusters on the market, to perform different functions and match various constraints.

In this thesis the propulsion system has been designed to perform position manoeuvres, thus a cold gas propulsion system has been chosen. This system is the simplest, cheapest and most reliable on the market. It is composed by some propellant storage tanks and a number of nozzles disposed around the spacecraft, which expel the gas thanks to control valves.

The gas used in this work is the hydrazine ( $N_2H_4$ ) and the thrusters are disposed as shown in figure 2.4.

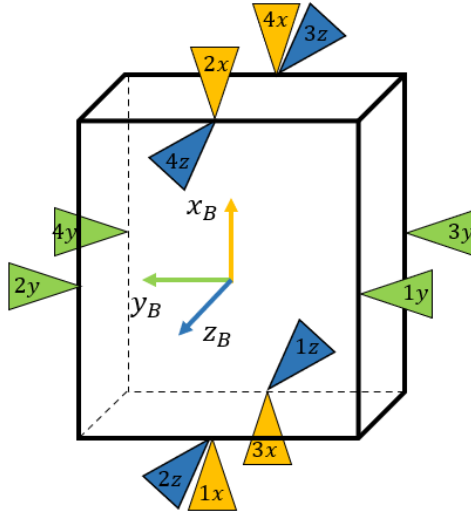


**Figure 2.4:** Disposition of the thrusters

The thrusters are mono-directional and can produce forces along the satellite's body axis (see table 2.2). They are always activated in couples with the same direction, otherwise a torque will be generated compromising the attitude of the spacecraft. For this reason, the proposed propulsion system could also perform attitude manoeuvres and help the reaction wheels when they are saturated, but this case is not considered in this work.

Force's direction	Thrusters used
$+x$	$1x, 3x$
$-x$	$2x, 3x$
$+y$	$1y, 3y$
$-y$	$2y, 4y$
$+z$	$1z, 3z$
$-z$	$2z, 4z$

**Table 2.2:** Distribution of forces along the body axes

The thrusters adopted in this work are the 20N chemical monopropellant thrusters developed by ArianeGroup. These thrusters are very reliable, in fact they have been used since the 80's in different missions and spacecrafts, like *METOP 1-3*, *Herschel* and *NGSAR* [25]. They are equipped with a double stage flow control valve to regulate the fuel supply, and a redundant catalyst bed heater to ensure a better start up.

Table 2.3 sums up the main characteristic of these thrusters.

Characteristics	
Thrust range	$7.9 \div 24.6$ N
Supply pressure range	$5.5 \div 24$ bar
Nominal mass flow range	$3.2 \div 10.4$ g/s
Nominal specific impulse range	$222 \div 230$ s
Minimum impulse bit range	$0.238 \div 0.685$ Ns
Nozzle area ratio	60
Mass	0.65 kg

**Table 2.3:** Characteristics of the 20N chemical monopropellant thruster [25]

## Chapter 3

# Flexible Appendages Model

As already said in Chapter 1, to reduce the launch costs it is necessary to decrease the spacecraft's mass. The main drawback of this operation is the achievement of a less rigid structure. Therefore, a new task arises for the attitude control system: the elimination of vibrations.

Vibrations can be suppressed with dampers like piezoelectric actuators, as proposed from De Gennaro [16]. These actuators consist of piezoelectric films bonded to the structure, increasing the stiffness and the internal damping. With the aid of dampers, the time needed to damp out the oscillations is largely reduced, and the workload on the control system is lighter.

Since this work aim to study the robustness of the proposed control systems in adverse scenarios, no dampers are considered.

In this chapter, the flexible appendages are studied in order to understand how they affect the spacecraft attitude dynamics. The first section presents the alterations to the satellite's dynamics seen in Subsection 2.3.2. Secondly, different kinds of forcing are proposed to further solicit the base satellite.

In this thesis, the flexible parts considered are two 1-DoF solar arrays, that can be deployed as shown in figure 3.1.

### 3.1 Mathematical model of a flexible satellite

The base satellite attitude dynamics has been already described by the Euler's equation 2.13, but the satellite was threaten as a rigid body. Considering the flexible appendages, the dynamics of the spacecraft becomes more complicated and strongly non linear, and can be described as follows:

$$J_{sc}\boldsymbol{\omega}_B + \delta^T \ddot{\boldsymbol{\eta}} = \mathbf{T}_{ext} + \mathbf{u} - \boldsymbol{\omega}_B \times (J_{sc}\boldsymbol{\omega}_B + J_{RW}\boldsymbol{\omega}_{RW} + \delta\dot{\boldsymbol{\eta}}) \quad (3.1)$$

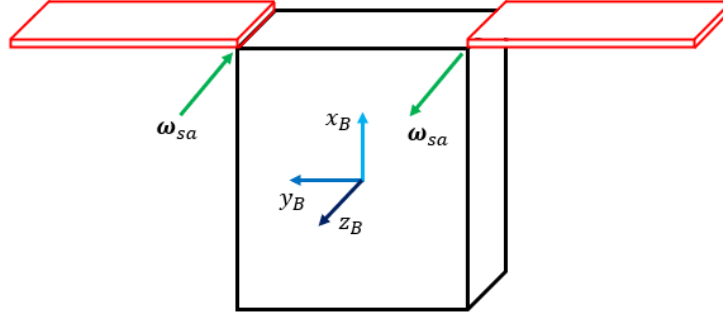


**Figure 3.1:** Solar arrays deployment

$$\ddot{\boldsymbol{\eta}} + C\dot{\boldsymbol{\eta}} + K\boldsymbol{\eta} = -\delta\dot{\boldsymbol{\omega}}_B \quad (3.2)$$

Equation 3.1 describes the attitude dynamics of the satellite with flexible appendages. The term  $\boldsymbol{\eta}$  represents the modal coordinate vector of the flexible satellite, and can be computed by equation 3.2. The other new terms w.r.t. equation 2.13 that appear in equations 3.1 and 3.2 are the following:

- $J_{sc}$  is the symmetric inertia matrix of the whole spacecraft, given by the sum of the base satellite inertia and the solar arrays inertia matrix;
- $\delta$  is the coupling matrix between the elastic and rigid structures;
- $C$  is the solar arrays dumping matrix;
- $K$  is the solar arrays stiffness matrix.

Matrices  $C$  and  $K$  are both diagonal and they are functions of the natural frequencies  $f_n$ , the corresponding dampings  $\zeta$  and the number  $N$  of elastic modes considered. Hence, these matrices depend by the spacecraft's geometry and materials, and can be computed as follows:

$$C = \begin{bmatrix} 2\zeta_1 f_{n_1} & & \\ & \ddots & \\ & & 2\zeta_N f_{n_N} \end{bmatrix} \quad K = \begin{bmatrix} f_{n_1}^2 & & \\ & \ddots & \\ & & f_{n_N}^2 \end{bmatrix}$$

The computation of natural frequencies and corresponding dampings requests a structural analysis that goes beyond the purpose of this work. These parameters have been taken from [16], considering four bending modes, and are summed in table 3.1.

Mode	$f_n$ (rad/s)	$\zeta$
1	0.7681	0.05607
2	1.1038	0.08620
3	1.8733	0.01283
4	2.5496	0.02516

**Table 3.1:** Parameters of the Flexible Dynamics

The solar arrays deployment represents a particular issue to the attitude dynamics. Firstly, during the passage from stowed to deployed configuration, the inertia matrix of the whole spacecraft changes, affecting the attitude control. Secondly, the reaction torques acting on the panels' hinges and their angular momentum during the transitory phase can affect the attitude dynamics. To analyze these two issues, some considerations on the deployment mechanism have to be done.

In stowed condition the solar arrays are aligned to spacecraft's sides on the  $x_B - z_B$  plane. Then they are deployed with a constant angular rate of 0.0785 deg/s, until they reach the desired position of  $90^\circ$  between the panel's surface and the  $x_B$  axis. This operation should take 20 seconds to be done. The deployment mechanism is the one proposed in [17] and shown in figure 3.2, due to its simplicity. It mainly consists of a torsion spring, which applies the torque to deploy the panel, and a paraffin actuator, which controls the angular rate. Once the panel has been deployed, a rigid joint locks it in the desired position. All the components of the deployment mechanism are considered ideal, thus there is no friction.

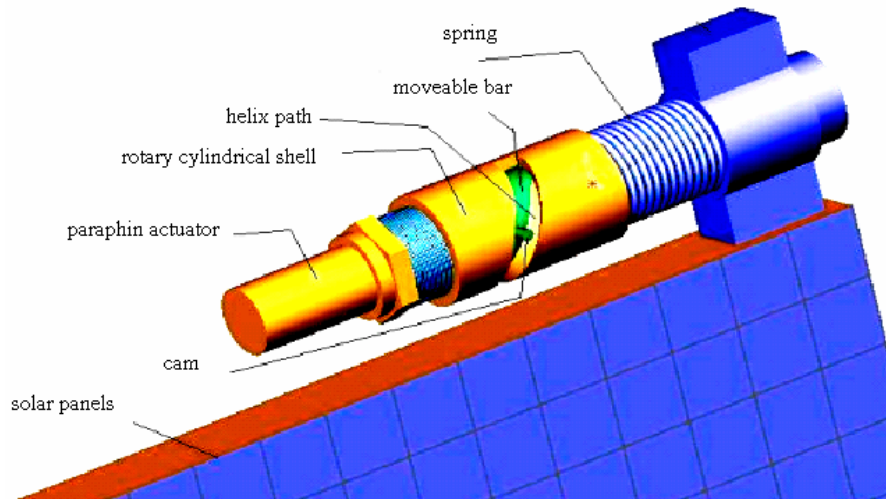


**Figure 3.2:** Solar arrays' deployment mechanism [17]

Regarding the first issue, table 3.2 resumes the spacecraft's dimensions in the two different configurations. The panels' thickness has been considered negligible and, for simplicity, the inertia tensor during the transitory phase has been computed as a linear variation of the inertia tensors in stowed and deployed condition.

	$l_x$ (m)	$l_y$ (m)	$l_z$ (m)
Stowed	1.38	1.04	1.58
Deployed	1.38	2.47	1.58

**Table 3.2:** Satellite's dimensions in stowed and deployed conditions

Eventually, for what concern the angular momentum of the panels and the reaction torques, the symmetry of the spacecraft allow us to neglect them in the dynamics equation. Considering the two panels are deployed in the same interval of time and with the same angular rates in modulus, the angular momentum vectors generated by this motion lie in  $z_B$  direction with opposite verses, thus they eliminate each other (see figure 3.1). The same thing happens to the reaction torques on the hinges.

This is the reason why these terms do not appear in equation 3.1.

## 3.2 External forces applied

In order to further solicit the system, a time sinusoidal forcing has been applied as external disturbance. This forcing can be considered as an unforeseen oscillation due to the model uncertainties, or just a wanted solicitation to test the robustness of the attitude control system. The forcing is in the following form:

$$F = A \sin(ft + \Phi)$$

where  $A$  is the amplitude of forcing,  $f$  is the frequency and  $\Phi$  is the phase. These three parameters have a big impact on the forcing behaviour, therefore different simulations have been run to choose the more suitable to the purpose of this work. The frequency chosen is the first natural frequency  $f_{n_1}$ , because it is the most critical. The phase does not have a great influence on the attitude control, thus has been considered null. Regarding the amplitude, if it is constant the system will never reach the desired attitude because of a residual oscillation, hence it has been chosen time dependant. In the majority of the scenarios studied in Chapter 5, the forcing amplitude is equal to  $\eta_1$ , the first component of the modal vector. Thus the forcing tends to zero when the first modal variable becomes null, and the system can reach the desired attitude with no residual oscillations.

Moreover, another term is added to equation 3.2, to couple the forcing to the attitude dynamics. This term is  $\delta^* \Delta \dot{\boldsymbol{\omega}}$ , where  $\delta^*$  is a fraction of the coupling matrix ( $\delta^* = 0.1 \cdot \delta$ ), and  $\Delta \dot{\boldsymbol{\omega}}$  is given by equation 3.3.

$$J_{sc} \Delta \dot{\boldsymbol{\omega}} = \mathbf{F} \quad (3.3)$$

To conclude the previous considerations, the attitude dynamics for a spacecraft with flexible appendages can be expressed by the equations 3.4.

$$\begin{cases} J_{sc} \boldsymbol{\omega}_B + \delta^T \ddot{\boldsymbol{\eta}} = \mathbf{F} + \mathbf{T}_{ext} + \mathbf{u} - \boldsymbol{\omega}_B \times (J_{sc} \boldsymbol{\omega}_B + J_{RW} \boldsymbol{\omega}_{RW} + \delta \dot{\boldsymbol{\eta}}) \\ \ddot{\boldsymbol{\eta}} + \mathbf{C} \dot{\boldsymbol{\eta}} + \mathbf{K} \boldsymbol{\eta} = -\delta \dot{\boldsymbol{\omega}}_B - \delta^* \Delta \dot{\boldsymbol{\omega}} \\ J_{sc} \Delta \dot{\boldsymbol{\omega}} = \mathbf{F} \\ \mathbf{F} = \eta_1 \sin(f_{n_1} t) \end{cases} \quad (3.4)$$

# Chapter 4

## Control Laws

In this chapter the adopted control laws are recalled. In the first section, the mathematical model of the base satellite is linearised in order to compute the state matrices needed to define the Linear Quadratic Regulator, which is presented in the second section. Then, in the third section, the Sliding Mode Control is implemented in the form of a First Order SMC and a Continuous Twisting SMC.

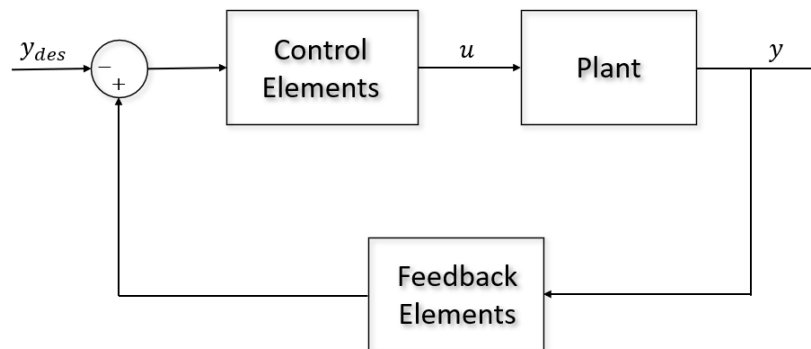


**Figure 4.1:** Closed-loop block diagram

All the control laws proposed are based on closed-loop architecture, to guarantee the system stability and robustness against external disturbances. The goal of these control laws is to allow the system to reach the desired conditions in a finite time.

As shown in figure 4.1, the control elements generate the control input  $u$ , which affects the plant. Then, the output  $y$  comes back through the feedback elements, and it is compared to the reference signal  $y_{des}$  to compute the error. Eventually, the control elements provide the new control input, based on the error measured.

In this way, the system can reduce the error by automatically adapting the input on the plant.

The control elements comprehend mainly the controller and the actuators. The controller has to evaluate the new input in order to reduce the error, and the actuators have to generate the new input on the plant. As previously said, the actuators considered in this work are reaction wheels and a propulsion system.

The feedback elements are the sensors, for simplicity treated as ideal sensors, thus all the states variables are known.

Lastly, the plant is where the dynamics and kinematics of the system is computed.

## 4.1 Mathematical model of the linearised system

As seen in sections 2.2 and 2.3, the spacecraft's dynamics for the attitude and position motions is described by non linear equations. In order to implement a Linear Quadratic Regulator, those equations have to be linearised. Hence, a Taylor series expansion around an equilibrium point is adopted, because both the attitude and the position dynamics equations are functions of two variables.

Considering  $x$  and  $u$  as general variables and a function  $g(x, u)$ , the first order Taylor expansion is the following:

$$g(x, u) = g(x_0, u_0) + \left. \frac{\partial g(x, u)}{\partial x} \right|_{x_0, u_0} (x - x_0) + \left. \frac{\partial g(x, u)}{\partial u} \right|_{x_0, u_0} (u - u_0) \quad (4.1)$$

Where the  $x_0$  and  $u_0$  denotes the equilibrium point.

At this point, with some derivations of the partial derivative, it is possible to derive a Linear Time Invariant system, in the state space representation:

$$\begin{cases} \dot{\mathbf{x}}(t) = \mathbf{A}\mathbf{x}(t) + \mathbf{B}\mathbf{u}(t) \\ \mathbf{y} = \mathbf{C}\mathbf{x}(t) + \mathbf{D}\mathbf{u}(t) \end{cases} \quad (4.2)$$

where  $\mathbf{x}$  is the state vector,  $\mathbf{y}$  the measured output and  $\mathbf{u}$  the control input. The matrices  $A, B, C$  and  $D$  are linearised in the neighbourhood of the equilibrium point, and they are constant.

These vectors and matrices depend by the dynamics equations, therefore they are different for the attitude and position models. The only thing in common is that for both models matrix  $C$  is chosen to be an identity matrix, and matrix  $D$  is null. Besides, the linear system follows two important assumptions: observability and controllability.

Observability is a characteristic of the pair  $A, C$  and means that all the states can be measured, thus there is no need of an observer (it is beyond the purpose of

this thesis).

In order to guarantee this assumption, an observability matrix is built:

$$\mathcal{O} = \begin{bmatrix} C \\ CA \\ CA^2 \\ \vdots \\ CA^{n_s-1} \end{bmatrix}$$

where  $n_s$  is the system's order.

The system is observable if equation 4.3 is verified.

$$\text{rank}(\mathcal{O}(A, B)) = n_s \quad (4.3)$$

Controllability, instead, is the capability of the system to guarantee that all the states can be controlled by the inputs  $u$ . It is a characteristic of the matrices  $A$  and  $B$ , and is verified if equation 4.4 holds.

$$\text{rank}(\mathcal{C}(A, B)) = n_s \quad (4.4)$$

where  $\mathcal{C}$  is the controllability matrix:

$$\mathcal{C} = [B \quad AB \quad A^2B \quad \dots \quad A^{n_s-1}B]$$

#### 4.1.1 Linearisation of position equations

Equation 2.4 can be written as  $\dot{\mathbf{r}} = f(\mathbf{r}, \mathbf{F})$ , where  $\mathbf{r} = [x, y, z]^T$  is the relative position vector between chaser and target, and  $\mathbf{F}$  is the thrust vector in the LVLH frame. The state vector is  $\mathbf{x} = [x, y, z, \dot{x}, \dot{y}, \dot{z}]^T$ , and the control input is  $\mathbf{F}$ .

Thus the matrices  $A$ ,  $B$  and  $C$  are the following.

$$A_{pos} = \begin{bmatrix} 0 & 0 & 0 & 1 & 0 & 0 \\ 0 & 0 & 0 & 0 & 1 & 0 \\ 0 & 0 & 0 & 0 & 0 & 1 \\ 0 & 0 & 0 & 0 & 0 & 2n \\ 0 & -n^2 & 0 & 0 & 0 & 0 \\ 0 & 0 & 3n & -2n^2 & 0 & 0 \end{bmatrix} \quad (4.5)$$

where  $n = \sqrt{\mu/r_t^3}$  is the orbital rate.

$$B_{pos} = \frac{1}{m_{sc}} \begin{bmatrix} 0 & 0 & 0 \\ 0 & 0 & 0 \\ 0 & 0 & 0 \\ 1 & 0 & 0 \\ 0 & 1 & 0 \\ 0 & 0 & 1 \end{bmatrix} \quad (4.6)$$

where  $m_{sc}$  is the spacecraft's total mass.

$$C_{pos} = \begin{bmatrix} 1 & 0 & 0 & 0 & 0 & 0 \\ 0 & 1 & 0 & 0 & 0 & 0 \\ 0 & 0 & 1 & 0 & 0 & 0 \\ 0 & 0 & 0 & 1 & 0 & 0 \\ 0 & 0 & 0 & 0 & 1 & 0 \\ 0 & 0 & 0 & 0 & 0 & 1 \end{bmatrix} \quad (4.7)$$

### 4.1.2 Linearisation of attitude equations

For what concern the attitude dynamics, considering  $\boldsymbol{\omega}_B$  as the angular velocity vector in body frame, and  $\mathbf{u}$  the control torque generated by the reaction wheels equation, 2.13 can be written as  $\dot{\boldsymbol{\omega}}_B = g(\boldsymbol{\omega}_B, \mathbf{u})$ . The state vector is a function of the Euler's angles and the angular velocities, thus  $\mathbf{x} = [\phi, \theta, \psi, \omega_{x_B}, \omega_{y_B}, \omega_{z_B}]^T$ , and the control input is  $\mathbf{u}$ .

Thus the matrices  $A$ ,  $B$  and  $C$  are the following.

$$A_{att} = \begin{bmatrix} 0 & 0 & n & 1 & 0 & 0 \\ 0 & 0 & 0 & 0 & 1 & 0 \\ -n & 0 & 0 & 0 & 0 & 1 \\ 0 & 0 & 0 & 0 & 0 & nJ_{321} \\ 0 & 0 & 0 & 0 & 0 & 0 \\ 0 & 0 & 0 & nJ_{213} & 0 & 0 \end{bmatrix} \quad (4.8)$$

where  $n$  is the orbital rate,  $J_{321}$  and  $J_{213}$  are given below:

$$J_{321} = \frac{J_{sc}(3,3) - J_{sc}(2,2)}{J_{sc}(1,1)} \quad J_{213} = \frac{J_{sc}(2,2) - J_{sc}(1,1)}{J_{sc}(3,3)}$$

$$B_{att} = \frac{1}{m_{sc}} \begin{bmatrix} 0 & 0 & 0 \\ 0 & 0 & 0 \\ 0 & 0 & 0 \\ 1 & 0 & 0 \\ 0 & 1 & 0 \\ 0 & 0 & 1 \end{bmatrix} \quad (4.9)$$

$$C_{att} = \begin{bmatrix} 1 & 0 & 0 & 0 & 0 & 0 \\ 0 & 1 & 0 & 0 & 0 & 0 \\ 0 & 0 & 1 & 0 & 0 & 0 \\ 0 & 0 & 0 & 1 & 0 & 0 \\ 0 & 0 & 0 & 0 & 1 & 0 \\ 0 & 0 & 0 & 0 & 0 & 1 \end{bmatrix} \quad (4.10)$$

## 4.2 Linear Quadratic Control

The LQR control is one of the most simple optimal controller, it is easy to calculate and is a stable and explicit controller. The main disadvantage is that it cannot work with constraints.

LQR is a static state feedback control, thus  $\mathbf{u}(t) = K\mathbf{x}(t)$ . The aim is to find  $K$  such that the system is stable, i.e. the matrix  $A_{cl} = A + BK$  has only eigenvalues with negative real part.

First thing to do is to define the cost function  $J_{\text{inf}}$ .

$$J_{\text{inf}} = \int_0^{\text{inf}} \mathbf{x}^T(\tau)Q\mathbf{x}(\tau) + \mathbf{u}^T(\tau)R\mathbf{u}(\tau)d\tau \quad (4.11)$$

This function governs the performance of the closed loop system, has two quadratic terms and two weighting matrices  $Q$  and  $R$ , where  $Q = Q^T$  is positive semidefinite and  $R = R^T$  is positive definite. This means that all the eigenvalues of  $Q$  and  $R$  are real positive.

Now the optimal control problem is to find  $\mathbf{u}(t) = K\mathbf{x}(t)$  that minimize  $J_{\text{inf}}$ , with the following constraint:  $\dot{\mathbf{x}} = A\mathbf{x} + B\mathbf{u}$ .

This optimal feedback law is given by:

$$K_{LQR} = -R^{-1}B^T P \quad (4.12)$$

where  $P$  is a positive definite matrix, solution of the algebraic Riccati equation 4.13.

$$A^T P + PA - PBR^{-1}B^T P = -Q \quad (4.13)$$

On MATLAB, the command `lqr` allow to resolve the Riccati's equation and to compute the matrix  $K_{LQR}$ . The only matrices needed are  $A$ ,  $B$ ,  $Q$  and  $R$ . Obviously, this matrices are different for the attitude control model and the position control model, thus two matrices  $K_{LQR}$  will be find.

The weighting matrices  $Q$  and  $R$  have a strong influence on the system, usually they are chosen to be diagonal and their elements depend by the constraints on the state variables and the control input. Let  $n_s$  be the system's order and  $m$  the number of rows of  $\mathbf{u}$ , then  $Q$  and  $R$  are respectively defined by equations 4.14 and 4.15.

$$Q = \begin{bmatrix} q_1 & & & \\ & q_2 & & \\ & & \ddots & \\ & & & q_{n_s} \end{bmatrix} \quad (4.14)$$

$$R = \rho \begin{bmatrix} r_1 & & & \\ & r_2 & & \\ & & \ddots & \\ & & & r_m \end{bmatrix} \quad (4.15)$$

where  $\rho$  is a trade off parameter of the system, between regulation and control effort ( $\rho = 1$  in this work), while  $q_i$  and  $r_i$  are defined by equation 4.16.

$$q_i = \frac{1}{t_{s_i} x_{i_{max}}^2} \quad r_i = \frac{1}{u_{i_{max}}^2} \quad (4.16)$$

With:

- $t_{s_i}$  the desired settling time of  $x_i$ ;
- $x_{i_{max}}$  a constraint on  $|x_i|$ ;
- $u_{i_{max}}$  a constraint on  $|u_i|$ .

In this work,  $Q$  is an identity matrix with dimensions equal to  $A$ , while  $u_{max}$  are the maximum available thrusts for the position model, and the saturation torques of the reaction wheels for the attitude model.

### 4.3 Sliding Mode Control

The Sliding Mode Control is a widely used control law for the non-linear system. It presents good robustness properties in case of model uncertainties, especially the First Order SMC.

The main concept of this control law is the implementation of a sliding surface  $\sigma$ , which is a subset of the state space. This surface is taken as a reference for the trajectory of the plant, which has to lie on it. Hence, a feedback law is design to force the trajectory towards the surface and, once the surface is reached, to stay close to it.

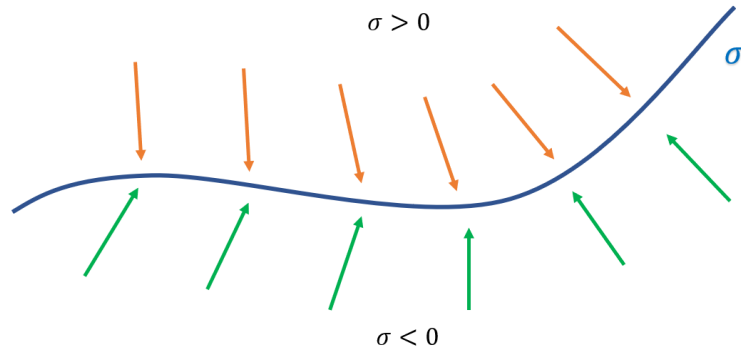


**Figure 4.2:** Graphic concept of the SMC

Figure 4.2 shows the SMC concept. The surface  $\sigma$  divides the geometric space into two subspaces: one where  $\sigma < 0$  and the other where  $\sigma > 0$ . When the

state trajectory is in one subspace, the control law has to push it in the opposite subspace, and when it crosses the surface, the trajectory is pushed back towards the first subspace. Thus, a sliding mode is generated.

There are different ways to design the sliding surface and the control law. The main aspect to consider is that the control input  $u$  has to drive the trajectory of the system towards the surface, hence a simple *sign* function could be used, like the one proposed in equation 4.17. With this control law it is clear that when the trajectory is in the subspace  $\sigma < 0$ , the control input is positive, and vice versa, forcing the trajectory towards the surface.

$$u = -k_\sigma \text{sign}(\sigma) \quad (4.17)$$

Regardless of the control law adopted, the SMC can be divided into two phases: the reaching phase and the sliding phase.

The reaching phase is the first phase, which starts at the initial state  $x(t_0)$  of the system and lasts until the trajectory of the plant reaches the sliding surface. In this phase the control law has to force the system towards the surface. The sliding phase, instead, is when the trajectory is already on the surface and the control law makes it slide around  $\sigma$ .

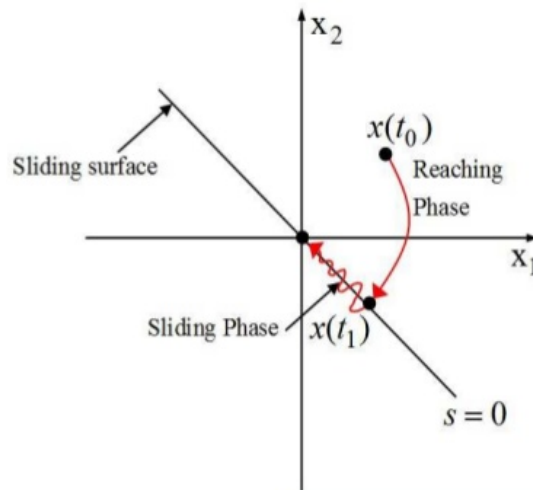


**Figure 4.3:** Sliding and reaching phases of the SMC. Credit to Liam Vile

These phases are shown in figure 4.3. If the initial state lies on the surface, only the last phase is performed, because the surface has already been reached.

### 4.3.1 First Order SMC

This control law is maybe the simplest SMC that can be implemented. The sliding surface  $\sigma$  and the control input  $u$  are presented in equations 4.18, where  $\omega_e$  is the angular velocity error,  $q_e$  is the vector part of the quaternion error, and  $C \in \mathbb{R}^{3 \times 3}$  is an identity matrix.

$$\begin{cases} u = -k_\sigma \text{sign}(\sigma) \\ \sigma = \omega_e + Cq_e \end{cases} \quad (4.18)$$

The control input is not really different from the one proposed in equation 4.17. The gain  $k_\sigma$  before the *sign* function, is a real number which increase the control input  $u$ , in order to force the reaction wheels to work in saturation condition. Therefore, this control law forces the system to work always on its limit, delivering the maximum torque available. This means a big control effort but also a great robustness.

One of the main drawbacks of the Sliding Mode Control, is the so-called chattering effect. This effect derive from the *sign* function, which generates discontinuity, causing the control input to switch continuously from one value to the opposite. The reaction wheels exert a continuous torque, therefore they do not fit well with a controller that provides discontinuous inputs. The consequence of using them under these conditions is a persistent noise on the command activity.

A solution to this problem could be the use of a continuous switching function, like the hyperbolic tangent proposed in [14]. This function allows to smooth the control action, decreasing the settling time but slightly increasing the steady state error. Nevertheless, the error accuracy is acceptable even for pointing manoeuvres.

Substituting the *sign* function with *tanh*, equation 4.19 is obtained, where  $\lambda \in \mathbb{R}$  is a parameter which mitigate the effect of the *tanh* function.

$$u = -k_\sigma \tanh(\lambda\sigma) \quad (4.19)$$

If  $\lambda$  is high, the *tanh* function tends to the *sign* function, as shown in figure 4.4. This means that the choice of  $\lambda$  depends by the trade off between accuracy and time response ( $\lambda = 10^2$  in this work).

In order to better understand the difference between the use of the *sign* function or the *tanh* function, a simple attitude manoeuvre has been done with the First Order SMC, using both functions.

In this simulation, no flexible appendages are considered. The state vector at the beginning of the simulation is  $\mathbf{x} = [0, 0, 0, 0, 0, 0]$ , and has to reach the desired state vector  $\mathbf{x}_{des} = [\pi/3, \pi/4, \pi/3, 0, 0, 0]$ .

As can be seen in figure 4.5, with the *sign* function the settling time is about 200 seconds, while with the other function is 150 seconds.

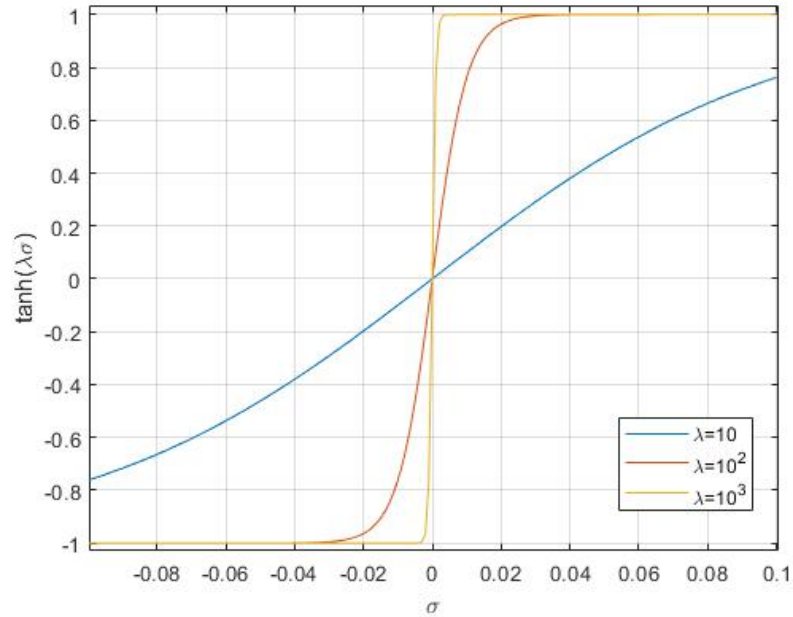


**Figure 4.4:** Effect of parameter  $\lambda$  on  $\tanh(\lambda\sigma)$  function

Moreover, figures 4.6a and 4.6b report the control torque of the same reaction wheel in the two different scenarios, showing a smoothest control when the *tanh* function is used. The other reaction wheels are not reported to not burden the presentation, but their behaviours are similar to the one shown in figure 4.6.

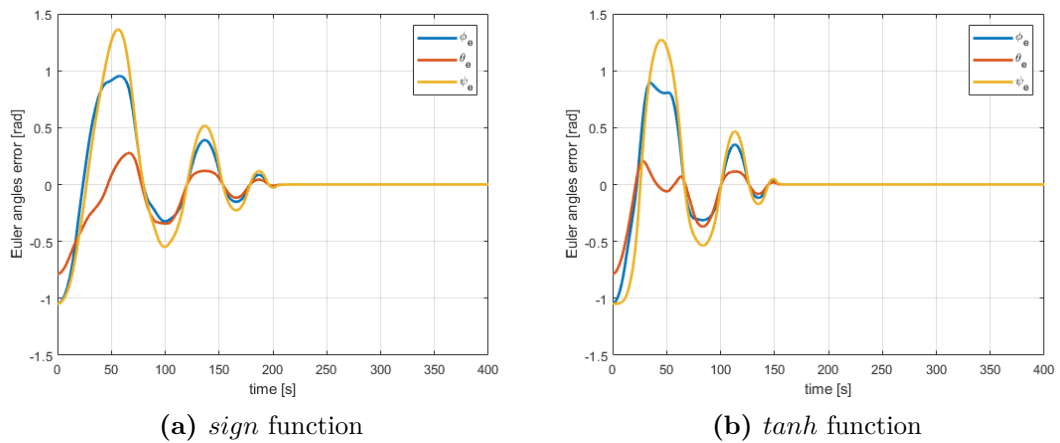


**Figure 4.5:** Euler's angles error in time

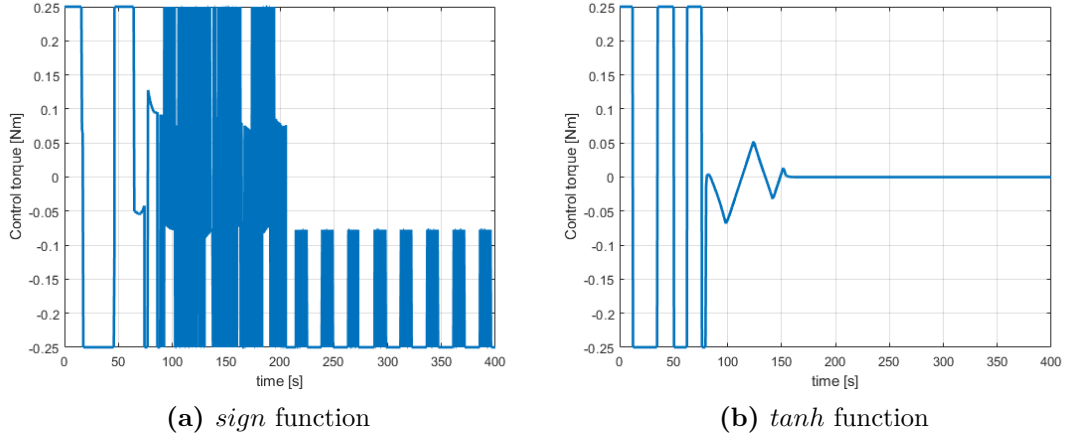


**Figure 4.6:** Control torques of one reaction wheels

### 4.3.2 Continuous Twisting SMC

The Continuous Twisting SMC is a high order SMC, which generates a continuous control input and ensures the convergence to zero of the sliding surface and its derivative, in finite time. Moreover, the controller is homogeneous.

Let equation 4.20 be an uncertain nonlinear control system, where  $\Delta(t)$ , the external disturbance, is a Lipschitz function, thus its derivative exist for  $t > 0$  and is bounded  $\dot{\Delta}(t) < \delta_p$ .

$$\begin{cases} \dot{\mathbf{x}}_1 = \mathbf{x}_2 \\ \dot{\mathbf{x}}_2 = \mathbf{u} + \Delta(t) \end{cases} \quad (4.20)$$

Considering  $\mathbf{x}_1$  and  $\mathbf{x}_2$  respectively as the vector part of the quaternion error  $q_e$  and the angular velocity error  $\omega_e$ , the Continuous Twisting control law can be derived as in [19].

$$\begin{cases} u = -k_1|q_e|^{\frac{1}{3}}\text{sign}(q_3) + -k_2|\omega_e|^{\frac{1}{2}}\text{sign}(\omega_e) + \nu \\ \dot{\nu} = -k_3|q_e|\text{sign}(q_e) - k_4|\omega_e|\text{sign}(\omega_e) \end{cases} \quad (4.21)$$

According to equations 4.21, the sliding surface  $\sigma = q_e$  and its derivative  $\dot{\sigma} = \omega_e$ . The integration of  $\nu$  increases the system order and allows the controller to compensate Lipschitz disturbances. As  $\sigma$  and  $\dot{\sigma}$ , also  $\nu$  converges to zero in finite time.

The parameters  $k_i$  are control gains as the ones proposed in table 4.1. To understand the process of the gains design, see [21], where the Lyapunov function proposed is positive definite and has a negative definite derivative.

In this work, the set of gains  $G_1$  has been chosen, because the other sets weren't enough adequate to ensure the system convergence.

Set	$k_1$	$k_2$	$k_3$	$k_4$
$G_1$	25	15	2.3	1.1
$G_2$	19	10	2.3	1.1
$G_3$	13	7.5	2.3	1.1
$G_4$	7	5	2.3	1.1

**Table 4.1:** Proposed control gains  $k$  [21]

The accuracy of the controller is guaranteed by the homogeneity property and the sliding motions expressed in 4.21. The accuracy is a function of the sampling interval  $\tau$  and, in steady state, it is  $|x_1| < \mu_1\tau^3$  and  $|x_2| < \mu_2\tau^2$ , where  $\mu_i$  are real positive numbers depending on the sets of gains, as reported in table 4.2.

Set	$\mu_1$	$\mu_2$
$G_1$	100	120
$G_2$	95	95
$G_3$	62	50
$G_4$	19	19

**Table 4.2:** Precision coefficient  $\mu$  [21]

# Chapter 5

## Simulations Results and Mission Scenarios

After all the considerations made in the previous chapters, the proposed control laws are now tested in different scenarios. The software used is MATLAB *Simulink*, and the simulations have been run with a fixed step of 100 Hz.

In the first section the case study is exposed and all the information needed to model the spacecraft are given.

In the second section the LQR<sup>1</sup> is adopted for a simulation with the linear system, while in the third section the LQR, the 1st-SMC<sup>2</sup> and the CT-SMC<sup>3</sup> are compared in a simple pointing manoeuvre, considering the non-linear system.

Then, in the last two sections, two mission scenarios are proposed:

- Crab Nebula observation;
- debris observation and capture.

### 5.1 Case study

The spacecraft modelled in this work is inspired to the *MicroSCOPE*<sup>4</sup>, a satellite designed and produced by CNES and ESA.

This satellite is prism-shaped with a rectangular base, it has a mass of 290 kg and two solar panels which can be deployed as reported in figure 5.1. The satellite is

---

<sup>1</sup>Linear Quadratic Regulator

<sup>2</sup>First Order Sliding Mode Control

<sup>3</sup>Continuous Twisting Sliding Mode Control

<sup>4</sup>Micro-Satellite a traînée Compensée pour l'Observation du Principe d'Equivalence

on a nearly circular orbit, with an eccentricity of  $5 \cdot 10^{-3}$  and an altitude of 720 km from the Earth's surface.

The dimensions of the base satellite and the single solar panels are reported in table 5.1, where  $l_x$ ,  $l_y$  and  $l_z$  are the lengths in the corresponding body frame axis (the solar panels are considered deployed and the thickness is negligible).

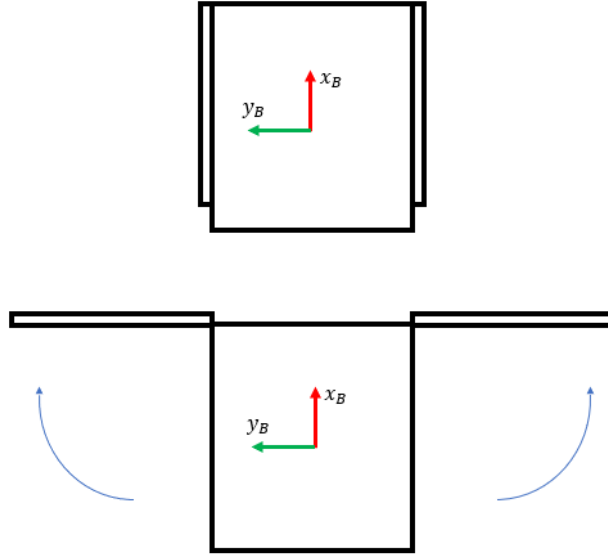


**Figure 5.1:** Graphic presentation of the solar arrays deployment

	Base satellite	Solar panel
$l_x$	1.38 m	/
$l_y$	1.04 m	0.715 m
$l_z$	1.58 m	1.58 m

**Table 5.1:** Satellite's dimensions

The solar panels have an area of  $1.13 \text{ m}^2$  each and a mass of 9.9 kg. Moreover, they can generate a power of about 99 W each in solar condition.

The Attitude Control System of the spacecraft is based on four reaction wheels in pyramidal configuration (see figure 2.3), with a skew angle of  $\beta = 30^\circ$ . The wheels chosen are the model  $RW4$  from Blue Canyon Technologies [24], which can exert a maximum torque of 0.25 Nm, a maximum momentum of 4 Nms and have a mass of 3.2 kg each.

The satellite is also equipped with a cold gas propulsion system for the position control, composed by twelve thrusters disposed all around the satellite, as shown

in figure 2.4. The thrusters chosen are the 20N chemical monopropellant thrusters from ArianeGroup [25], they have a thrust range of  $7.9 \div 24.6$  N and a mass of 0.65 kg each (see table 2.3 for more information).

### 5.1.1 Simulation of the linear system

In order to test the validity of the LQR, a simple pointing manoeuvre is performed, considering the closed loop linear system expressed in equation 4.2.

In this simulation, no flexible appendages are considered, the inertia tensor of the satellite is constant and the control law adopted is the LQR.

The state vector at the beginning of the simulation is  $\mathbf{x} = [0, 0, 0, 0, 0, 0]$ , and has to reach the desired state vector  $\mathbf{x}_{des} = [\pi/3, \pi/4, \pi/3, 0, 0, 0]$ .

Under this conditions, the poles of the matrix  $A_{cl}$  of the closed loop system are stable. In fact, the eigenvalues of this matrix are the following complex couples:  $(-0.0381 \pm 0.0379i)$ ,  $(-0.0416 \pm 0.0416i)$ ,  $(-0.0343 \pm 0.0342i)$ .

Figures 5.3a, 5.3b and 5.3c report the evolution of Euler's angles in time, while figure 5.3d shows the Euler's angle error. As can be seen, the system success to converge in about 160 seconds. The steady state error of the Euler's angles is notable and assumes the following values at the end of the simulation:  $[0.0281, -0.0011, -0.0271]$ .

The evolution of angular velocities is shown in figure 5.2.

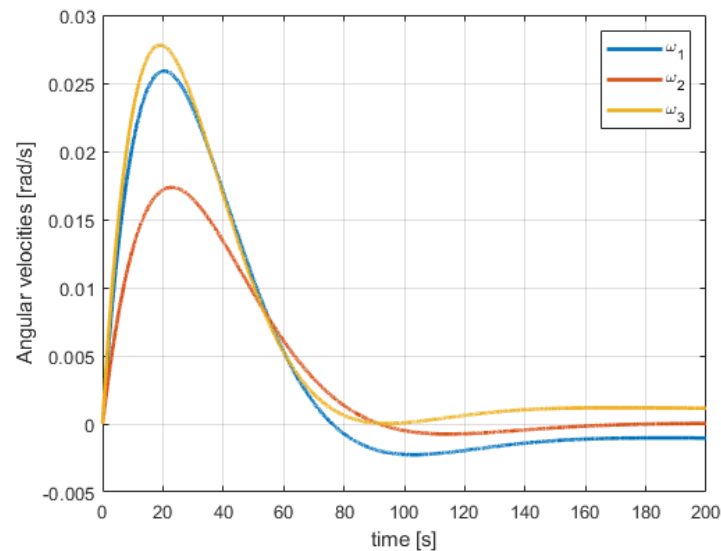
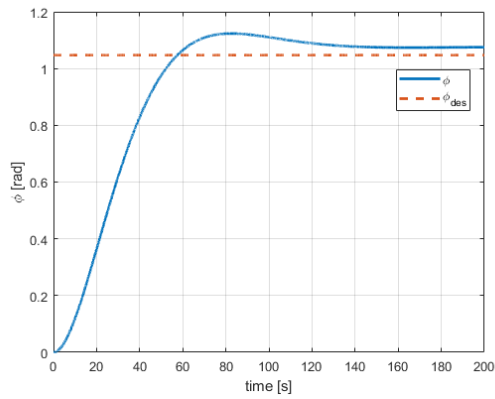
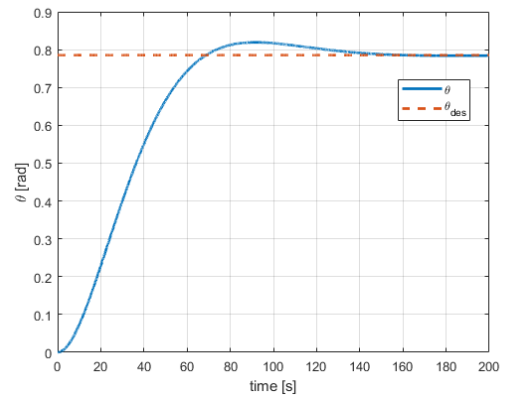


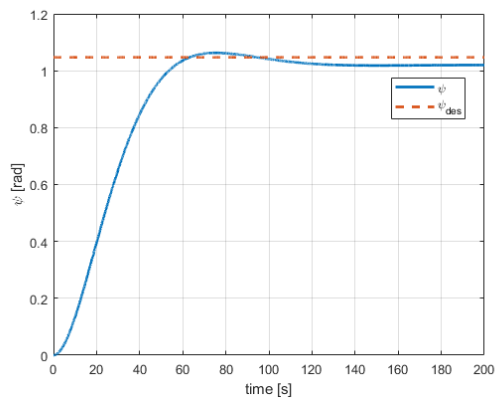
Figure 5.2: Linear system - Angular velocities in time with LQR



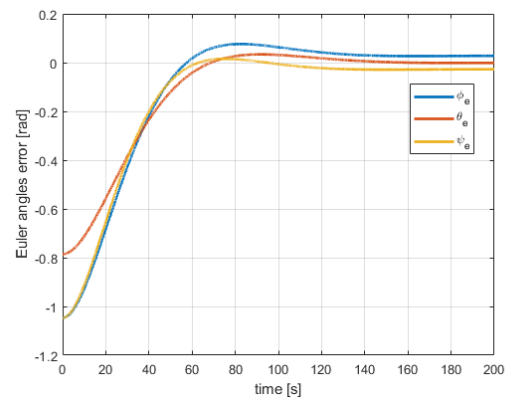
(a)  $\phi$  tracking



(b)  $\theta$  tracking



(c)  $\psi$  tracking



(d) Error tracking

**Figure 5.3:** Linear system - Euler's angles and error in time with LQR

## 5.2 Comparison between control laws

In order to understand which control law is the best for the satellite in exam, a pointing manoeuvre has been simulated. The 1st-SMC has been implemented with a gain  $k_\sigma = 10$ .

The manoeuvre is a rest to rest manoeuvre, therefore the initial and final angular velocities of the spacecraft are all null. The initial quaternion is the ideal one  $\mathbf{q}_{in} = [1, 0, 0, 0]$  and the final quaternion is  $\mathbf{q}_{des} = [0.8224, 0.2006, 0.5320, 0.0223]$ , which corresponds to the Euler's angle  $[\pi/6, \pi/3, \pi/4]$ .

The spacecraft is in stowed configuration at the beginning of the simulation, then, after 100 seconds, the solar arrays are deployed in 20 seconds.

The forcing applied to the system is in the form  $F = \eta_1 \sin f_1 t$ , where  $f_1$  is the first natural frequency and  $\eta_1$  is the first modal variable.

Figures 5.5a and 5.5b shows the evolution of quaternions for the 1st-SMC and the LQR. The 1st-SMC oscillates more but required a minor settling time (about 150 seconds), while the LQR needs 300 seconds to reach the desired quaternion. Moreover, the steady state error is in the order of  $10^{-8}$  with the 1st-SMC, and  $10^{-5}$  when the LQR is used.

This difference can be seen also in figures 5.6a and 5.6b where the angular velocities are reported. It is important to notice the different behaviour of the angular rates due to the nature of the control laws: the LQR is smoother than the 1st-SMC, even if the  $\tanh$  function is used. In fact, the LQR generates smoother control torques, as shown in figures 5.7a and 5.7b.

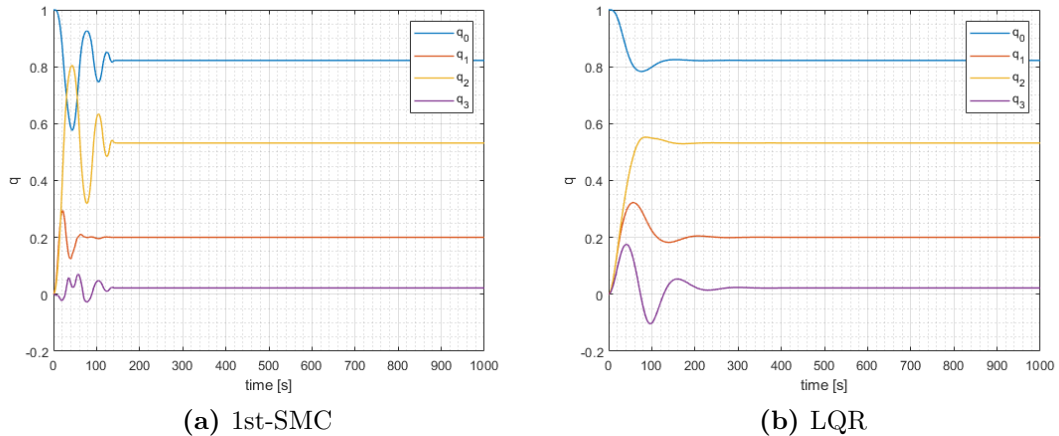
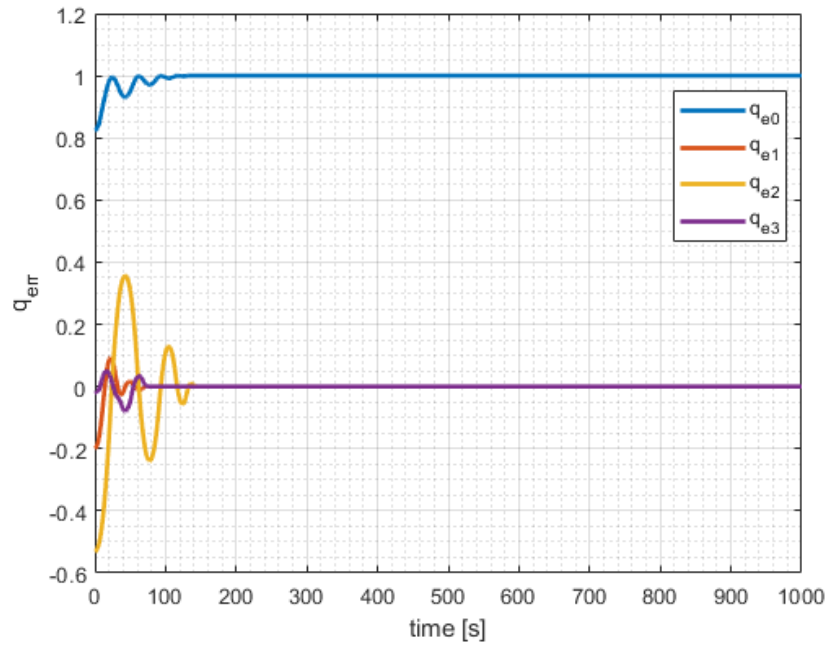
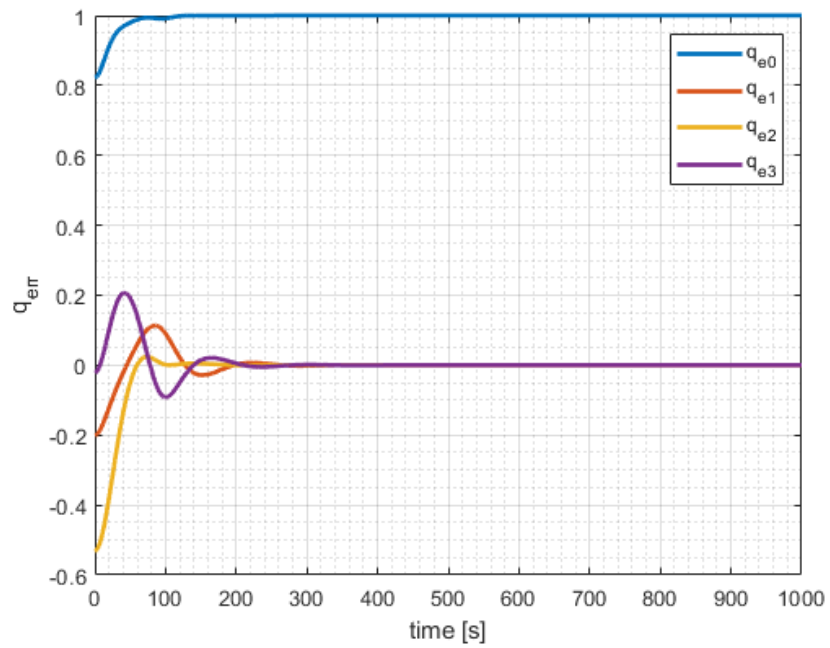


**Figure 5.4:** Comparison of quaternions in time

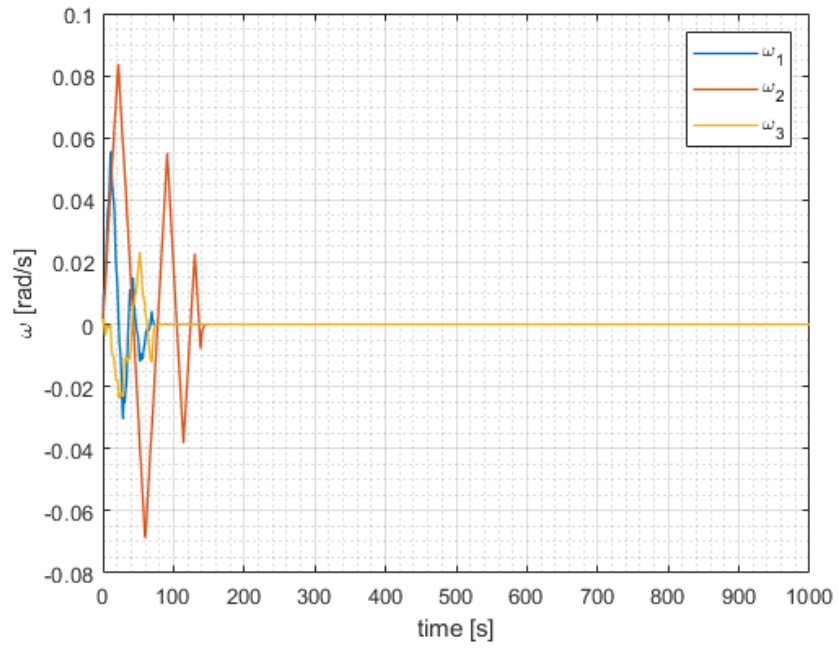


(a) 1st-SMC

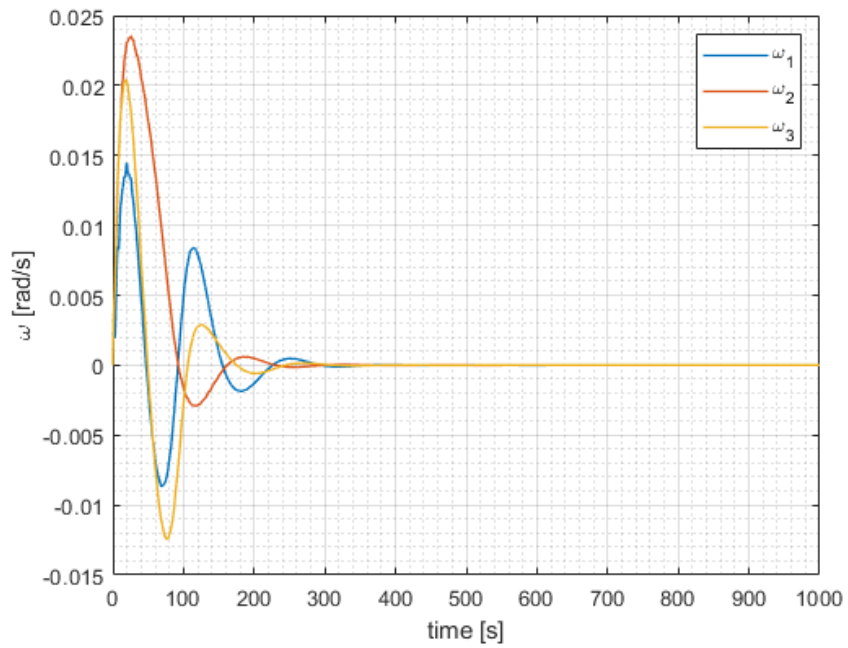


(b) LQR

**Figure 5.5:** Comparison of quaternion error in time

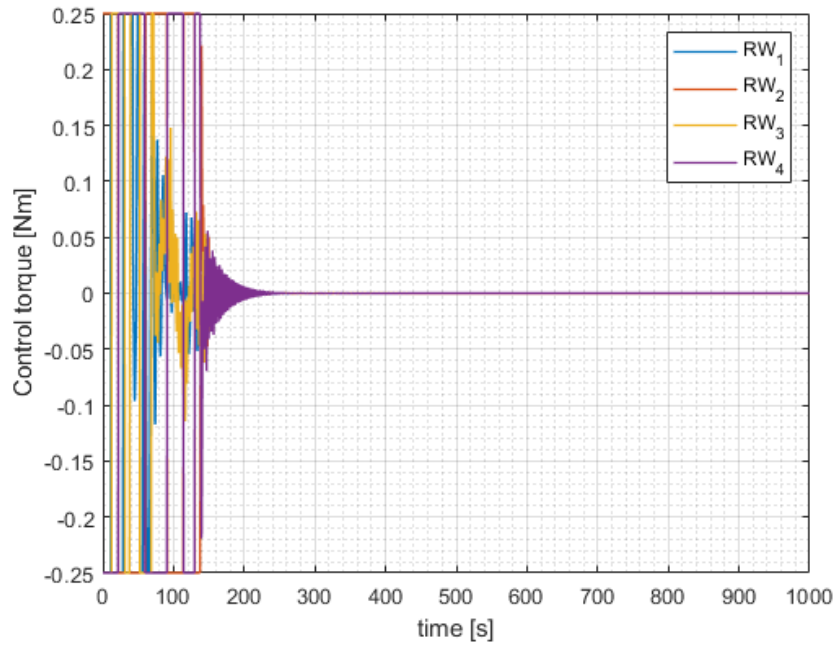


(a) 1st-SMC

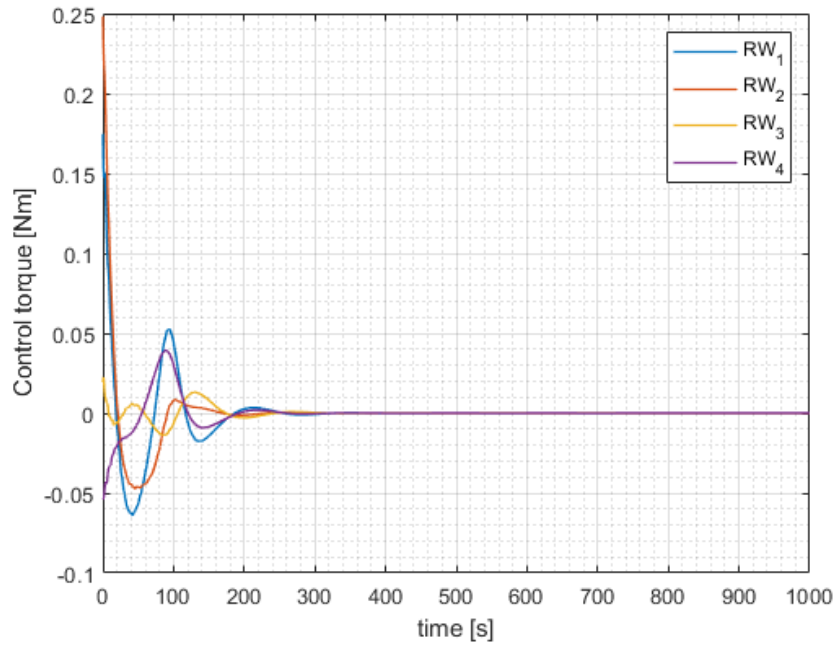


(b) LQR

**Figure 5.6:** Comparison of angular velocities in time

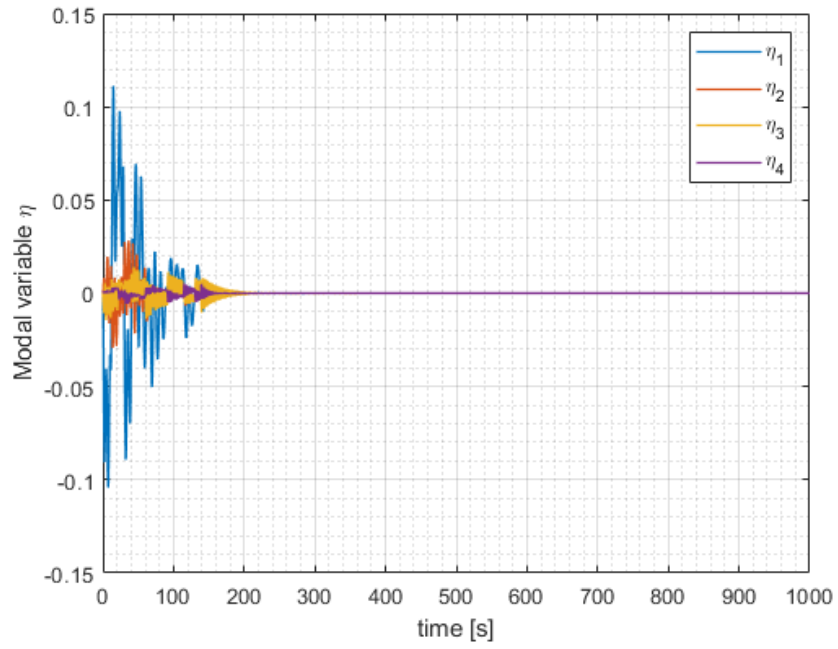


(a) 1st-SMC

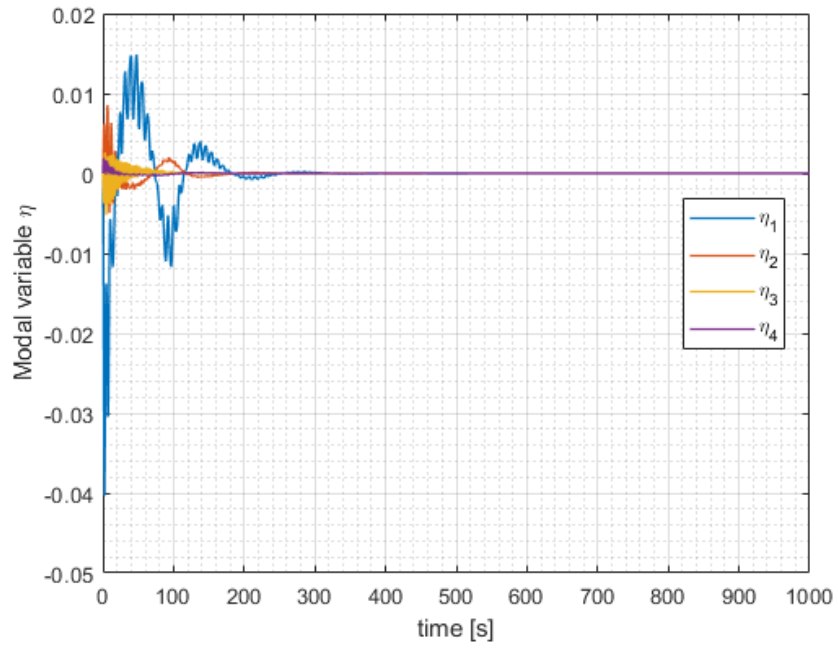


(b) LQR

**Figure 5.7:** Comparison of control torques in time



(a) 1st-SMC



(b) LQR

**Figure 5.8:** Comparison of modal variables in time

It is important to underline that the manoeuvre performed was a rest to rest manoeuvre, because the initial angular velocity vector has an important influence on the system response. In fact, when  $\omega_{in}$  is not null, the settling time increases, and the control system is not always able to reach the desired attitude, particularly when the LQR is used. With this control law, the system cannot converge if the angular velocities are higher than 0.001 rad/s, i.e. the majority of the cases when the satellite is not on an equilibrium point. Therefore, the LQR is not robust enough to succeed the missions presented in Section 5.3 and 5.4, and only the 1st-SMC is used.

The 1st-SMC, instead, shows a greater robustness when the angular velocities are not null. As example, the same pointing manoeuvre of the previous case has been simulated, but with the following initial condition:  $\omega_{in} = [0.05, 0.08, 0.07]$  rad/s.

As can be seen in figure 5.9, the system oscillates for a long time, until it reaches the desired attitude in about 5700 s. Due to the values of the angular velocities, the vibrations last more than the previous simulations (see figure 5.11), causing a stronger disturbance to the base satellite.

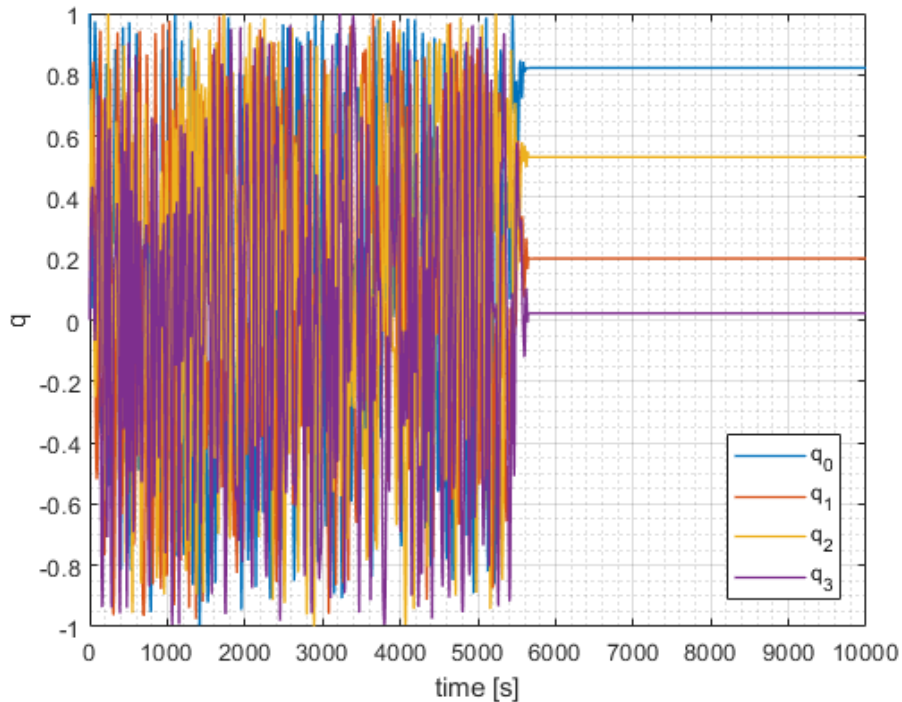


**Figure 5.9:** 1st-SMC - Quaternions in time

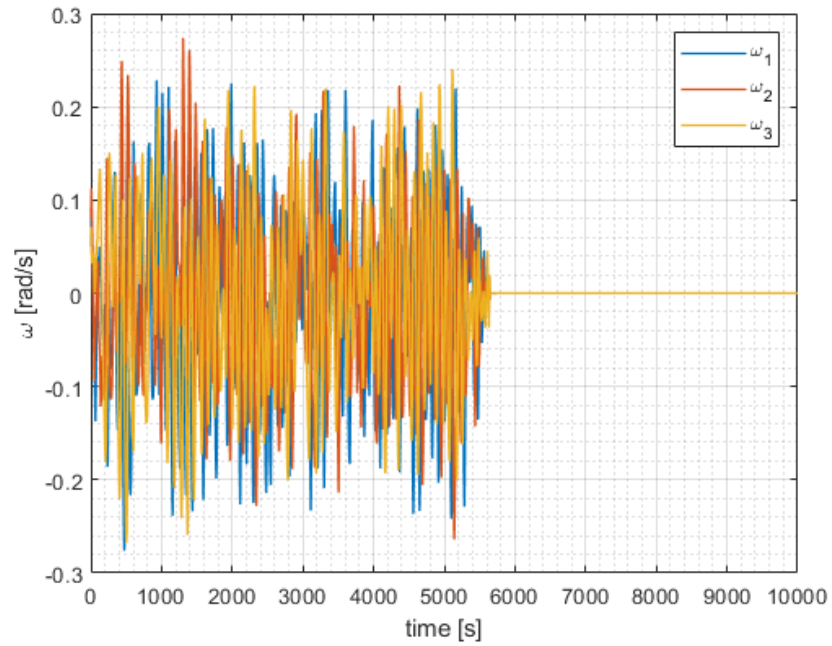


Figure 5.10: 1st-SMC - Angular velocities in time

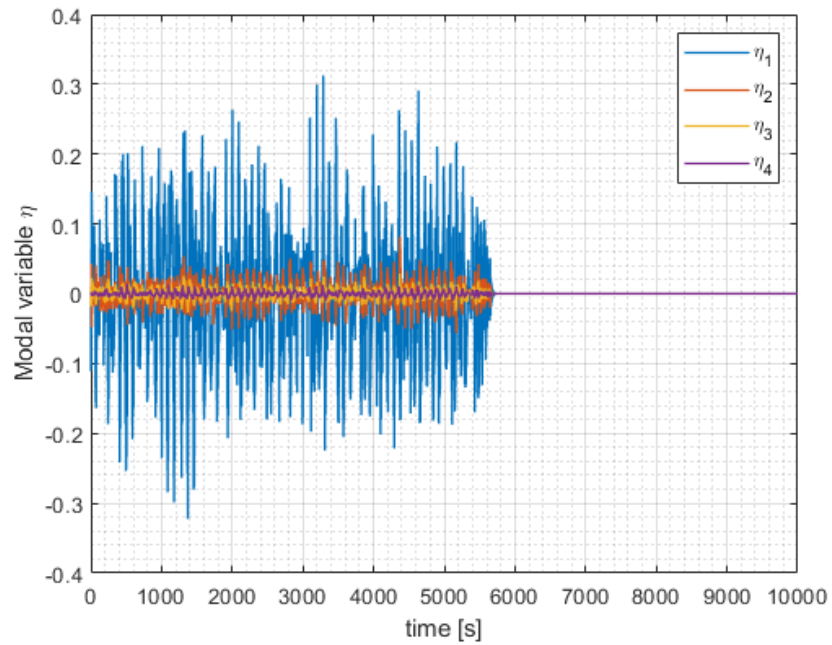


Figure 5.11: 1st-SMC - Modal variables in time

### 5.2.1 CT-SMC

The CT-SMC needs some considerations apart. Considering the initial conditions  $\mathbf{q}_{in} = [1,0,0,0]$  and  $\boldsymbol{\omega}_{in} = [0,0,0]$ , and the desired conditions  $\mathbf{q}_{des} = [0.8224, 0.2006, 0.5320, 0.0223]$  and  $\boldsymbol{\omega}_{des} = [0,0,0]$ , a simulation with the CT-SMC has been done.

The set of gain used is  $G_1$  from table 4.1, because with the other gains the system modelled in this work does not converge.

In figures 5.12 and 5.13 is reported the evolution of quaternions and quaternion error in time, but, as can be seen in figure 5.14, the system needs control torques up to 2 Nm, way more than the maximum control torque available (0.25 Nm).

With the limitation of the reaction wheels adopted in this work, the system cannot converge.

This means that the control authority of the modelled satellite is not appropriate for the implementation of the CT-SMC. For this reason, the CT-SMC has not been used in the mission scenarios of Sections 5.3 and 5.4.

A solution to this problem could be the usage of the thrusters, which can exert higher torques. In fact, the thrusters have a maximum thrust of 24.6 N and they are disposed in couples on the sides of the satellite, therefore they can produce torques up to 26 Nm. However, this scenario is not considered, and the propulsion system is only used for the position control.

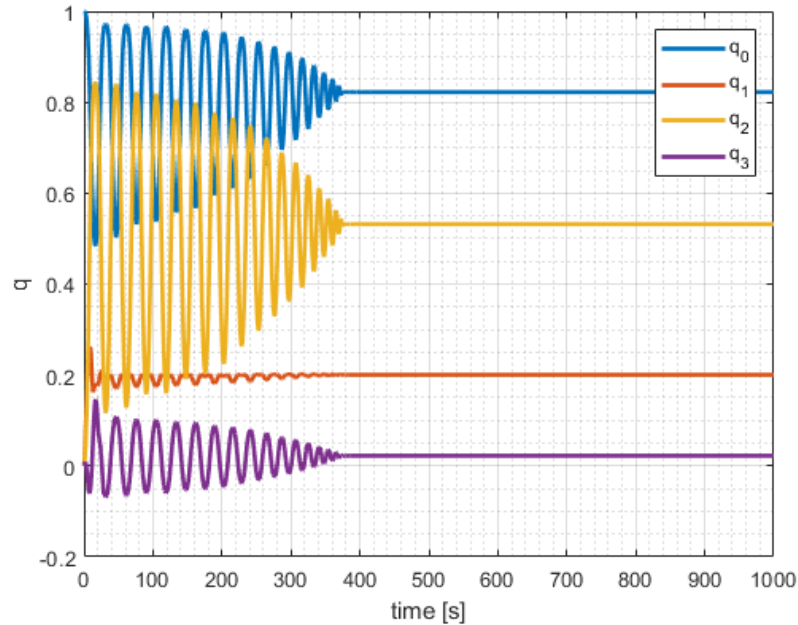


**Figure 5.12:** CT-SMC - Quaternions in time

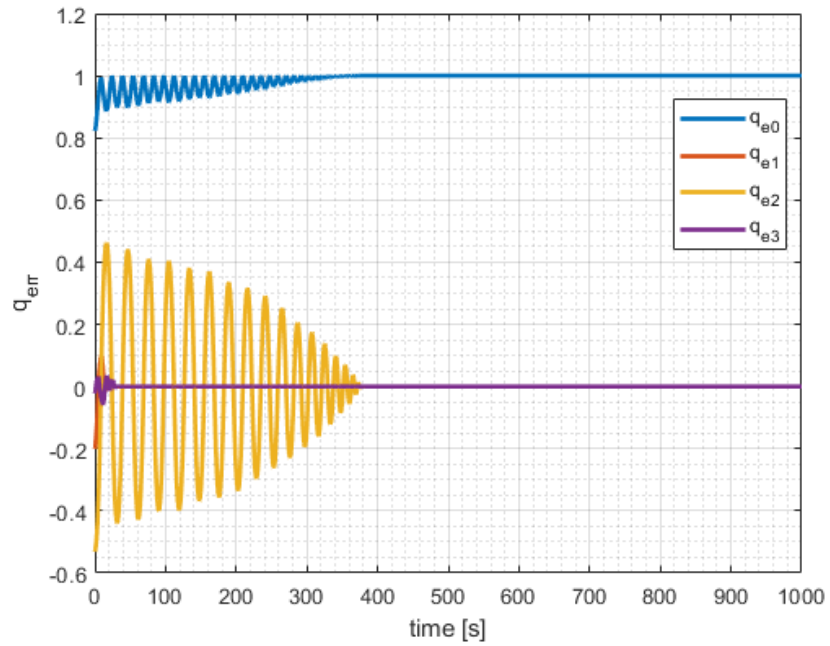


Figure 5.13: CT-SMC - Quaternion error in time

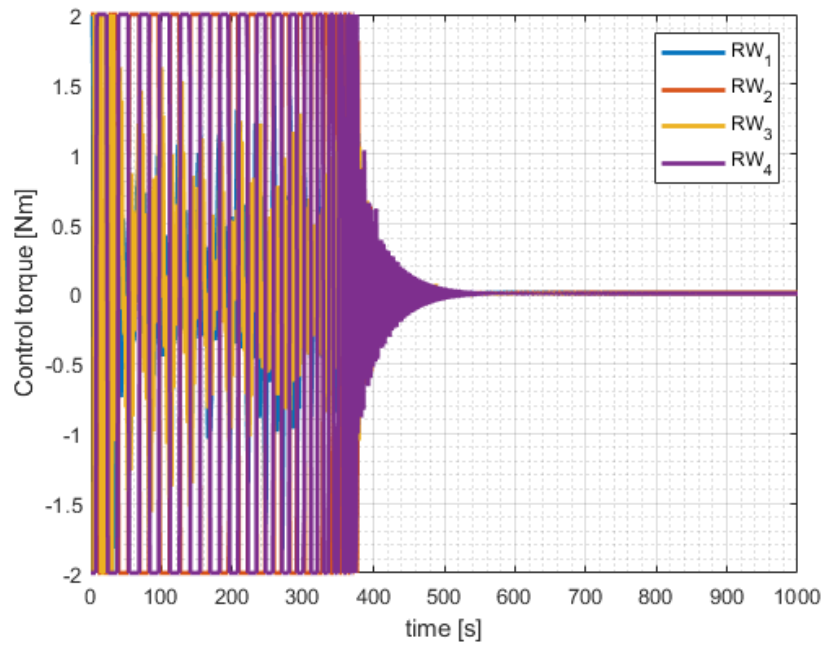


Figure 5.14: CT-SMC - Control torques in time

### 5.3 Crab Nebula observation mission

This mission scenario is not really different from a simple pointing manoeuvre such those viewed in Section 5.2, but with the addition of a second manoeuvre to align to the ideal quaternion  $\mathbf{q}_{id} = [1,0,0,0]$ . The goal of the mission is to observe the Crab Nebula, imagining to take some photos or collect other data. Then the satellite has to align to the ECI<sup>5</sup> frame in order to send the data to other satellites or to a ground station.

At the beginning of the mission, the satellite has just been inserted in the final orbit, therefore it has an initial angular velocity vector  $\boldsymbol{\omega}_{in} \neq 0$  and a detumbling operation is required.

The initial condition are here summarized:

- initial attitude  $\mathbf{q}_{in} = [0.7886, 0.2343, 0.5180, 0.2343]$ , which corresponds to the Euler's angle  $[\pi/3, \pi/4, \pi/3]$ ;
- initial angular velocity  $\boldsymbol{\omega}_{in} = [0.1, 0.01, 0.05]$  rad/s.

After the detumbling, the satellite has to point towards the Crab Nebula, thus it has to align to the desired quaternion  $\mathbf{q}_{des} = [0.9214, 0.1029, 0.0416, 0.3725]$  with null angular velocities. These two manoeuvres are performed together.

In the meanwhile, the solar arrays are deployed at the time  $t_d = 100$  s.

After 650 seconds from the beginning of the simulation, the satellite is assumed to have collected enough data, thus it can point to the ideal quaternion.

The control law used in this mission is the 1st-SMC, with the *tanh* function as proposed in equation 4.19. The forcing has amplitude equal to the first modal variable  $\eta_1$ , frequency equal to the first natural frequency and phase null.

As can be seen from figures 5.15 and 5.16, the satellite success to point towards the Crab Nebula in about 300 seconds, then it aligns with the ideal quaternion in 60 seconds. The residual error is  $[1.0000, 1.6811 \cdot 10^{-11}, 6.2504 \cdot 10^{-11}, 6.6658 \cdot 10^{-8}]$ .

The evolution of angular velocities is reported in figure 5.17. The first component of the angular velocity vector is the one that reaches the highest values, but  $\omega_3$  needs more time to be damped.

Figure 5.19 shows the command activity of the reaction wheels. As can be seen, the wheels switch very fast and have to work on their maximum torque for long period of time. This means that the manoeuvre could take fewer time if higher maximum torques would be available.

For what concern the modal variable  $\boldsymbol{\eta}$  (figure 5.20), the first component is the most solicited, and vibrations take place every time the satellite rotates around his

---

<sup>5</sup>Earth Centered Inertial

axis. Besides, vibrations continue even after the satellite has reached the desired attitude, and needs about 70 or even 90 seconds more to be damped.

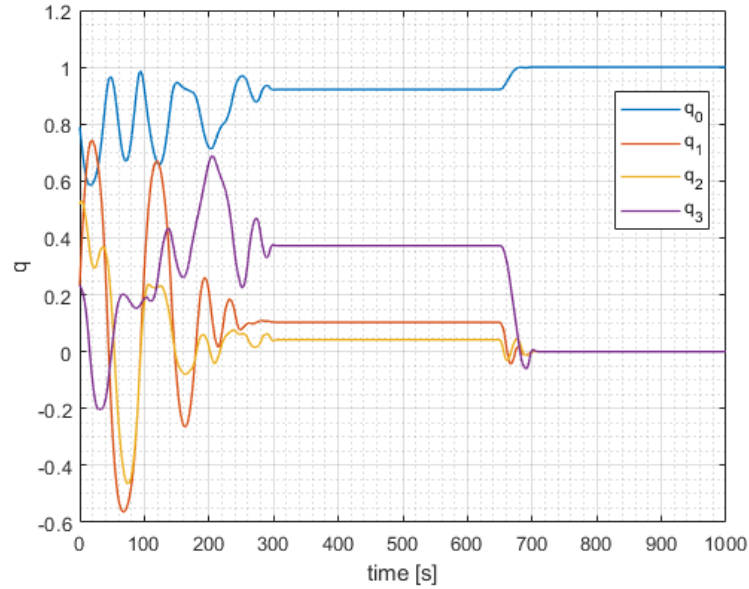


**Figure 5.15:** Crab Nebula mission - Quaternions in time

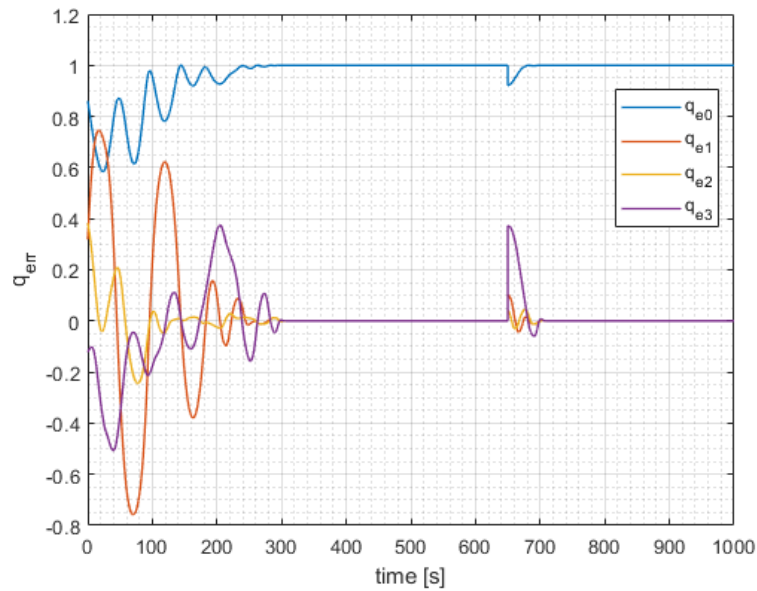


**Figure 5.16:** Crab Nebula mission - Quaternion error in time

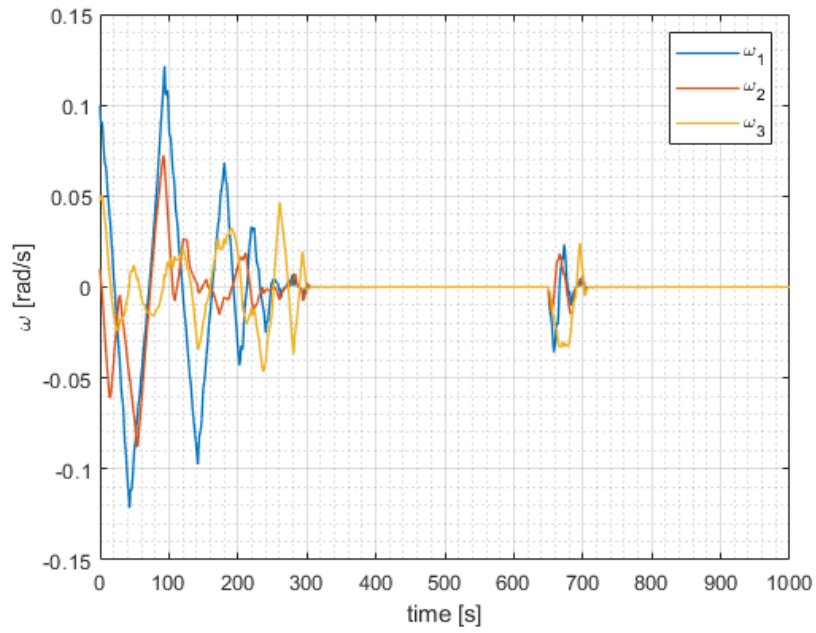


Figure 5.17: Crab Nebula mission - Angular velocities in time

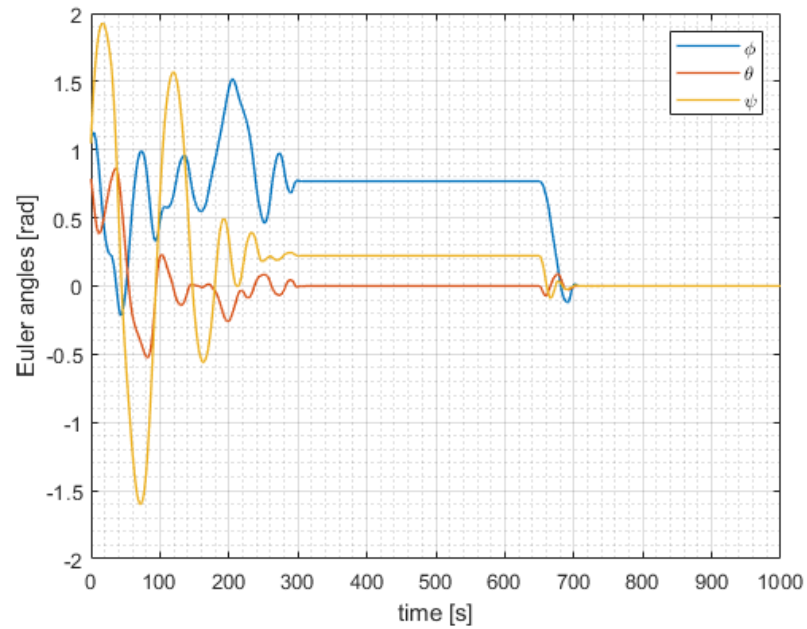


Figure 5.18: Crab Nebula mission - Euler's angles in time

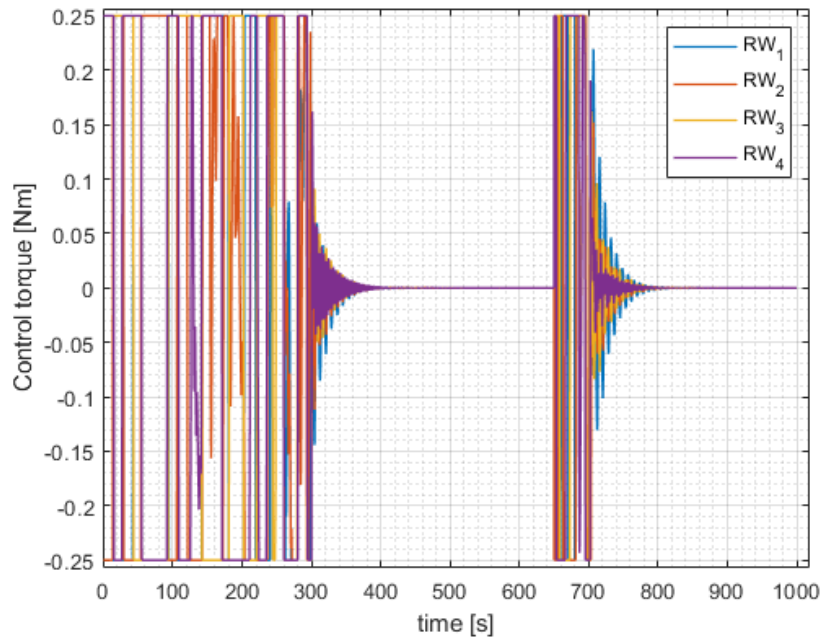


Figure 5.19: Crab Nebula mission - Control torques in time

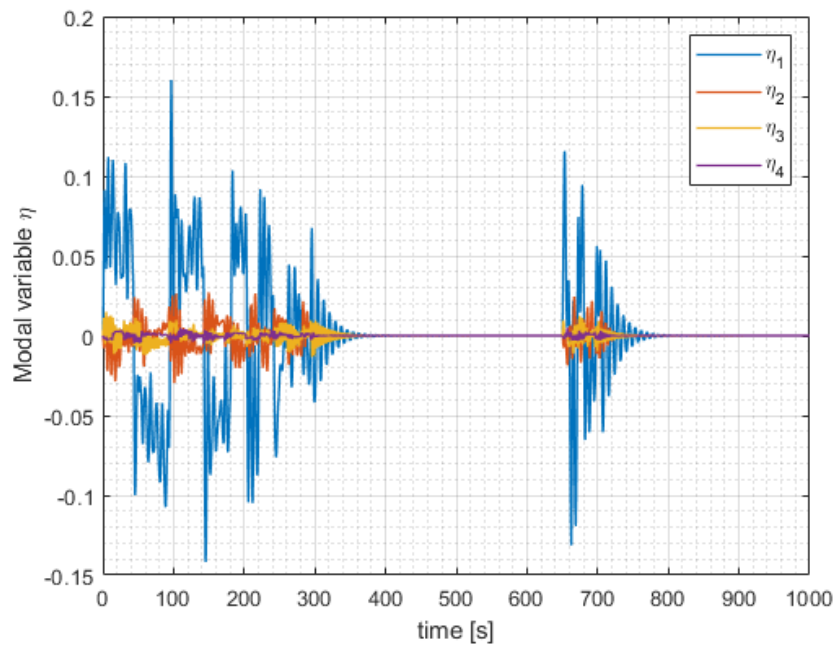


Figure 5.20: Crab Nebula mission - Modal variables in time

## 5.4 Debris observation and capture mission

In this mission the satellite has to perform several manoeuvres, in order to approach to a debris and capture it. The mission can be divided into two phases:

- observation phase;
- capture phase.

In the observation phase the satellite has to orientate itself in order to observe the debris and come closer to it with two radial boosts. The first radial boost occurs after 300 s from the beginning of the simulation, while the second one is 300 s after the first boost.

In the capture phase the chaser has to operate a last radial boost in order to arrive at a distance of 1 m from the target, then it has to capture the target and rotates itself in order to come back to the initial attitude.

The attitude control system is based on the 1st-SMC with a gain  $k_\sigma = 10$ , because in Section 5.2 has been shown to be the most robust, while the LQR is used for the position control. For the entire duration of the mission, the satellite has the solar arrays deployed, and the forcing applied is  $F = \eta_1 \sin f_1 t$ .

### 5.4.1 Observation phase

In this phase the initial attitude conditions are the ideal quaternion and the following angular velocities:  $\boldsymbol{\omega}_{in} = [0.01, 0.05, 0.02]$  rad/s. The chaser and the target are on two different orbit, with a relative position given by the initial position vector  $\mathbf{p}_{in} = [-5000, 0, 0]$  m, and a relative velocity null. These position and velocity are referred to the LVLH frame of the target.

The attitude control system of the chaser has to reach the desired quaternion  $\mathbf{q}_{des} = [0.8365, -0.1294, 0.2241, 0.4830]$  before the first boost, and keep it till the capture. With the first boost the position has to fall to  $\mathbf{p}_1 = [-2000, 0, 0]$ , and with the second one  $\mathbf{p}_2 = [-200, 0, 0]$ , keeping the relative velocity null after each manoeuvres.

Figure 5.21 shows that the attitude control system can reach the desired orientation in 200 s, even if the vibrations continue till 250 s, as can be seen in figure 5.24.

Looking at the evolution of position and velocity in figures 5.22 and 5.23, the LQR well control the radial boosts, and the two manoeuvres required less than 50 s each.

Figures 5.25 and 5.26 show the required control torques and thrusts. As expected, the reaction wheels have to work at their maximum torque during the attitude manoeuvre. Even the thrusters have to exert their maximum thrust during the radial boost, but for a short period of time, saving fuel for the next boosts.

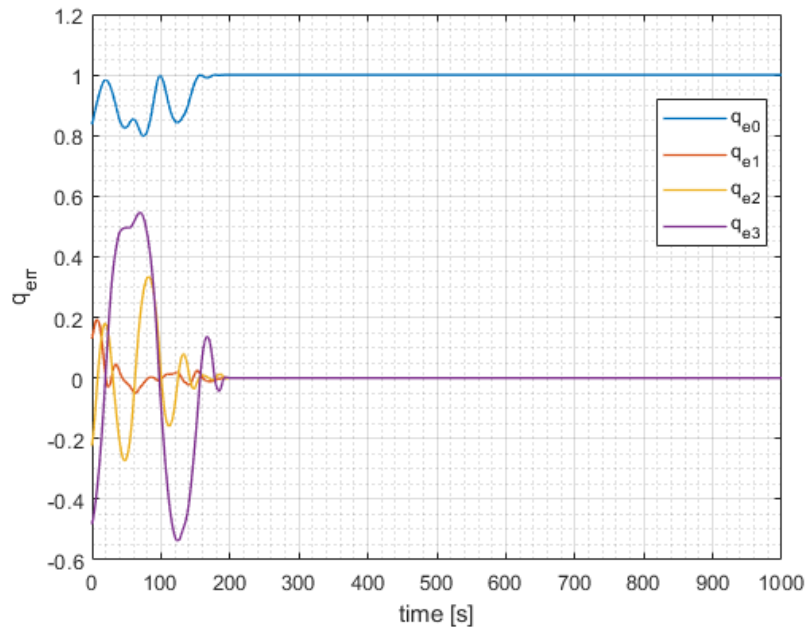


Figure 5.21: Observation phase - Quaternion error in time

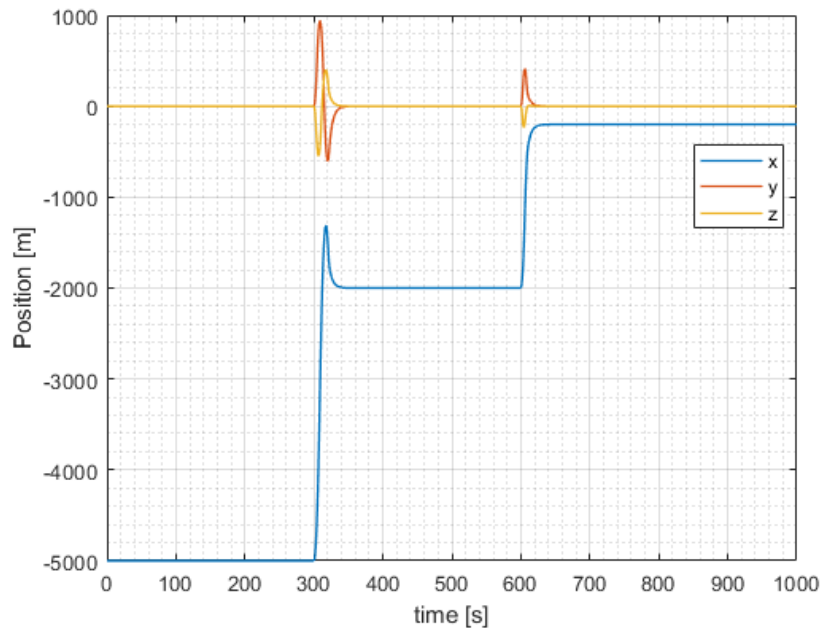


Figure 5.22: Observation phase - Evolution of position in time

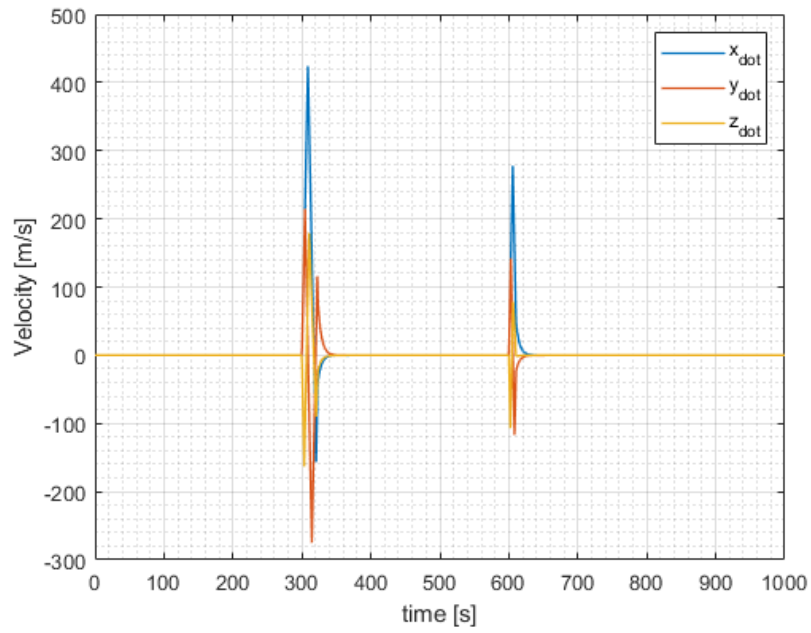


Figure 5.23: Observation phase - Evolution of velocity in time

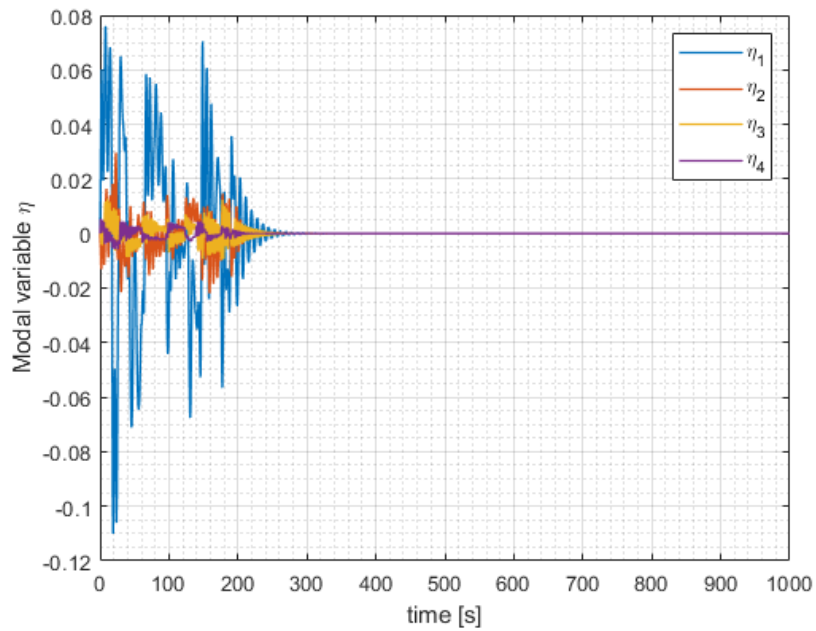


Figure 5.24: Observation phase - Modal variables in time

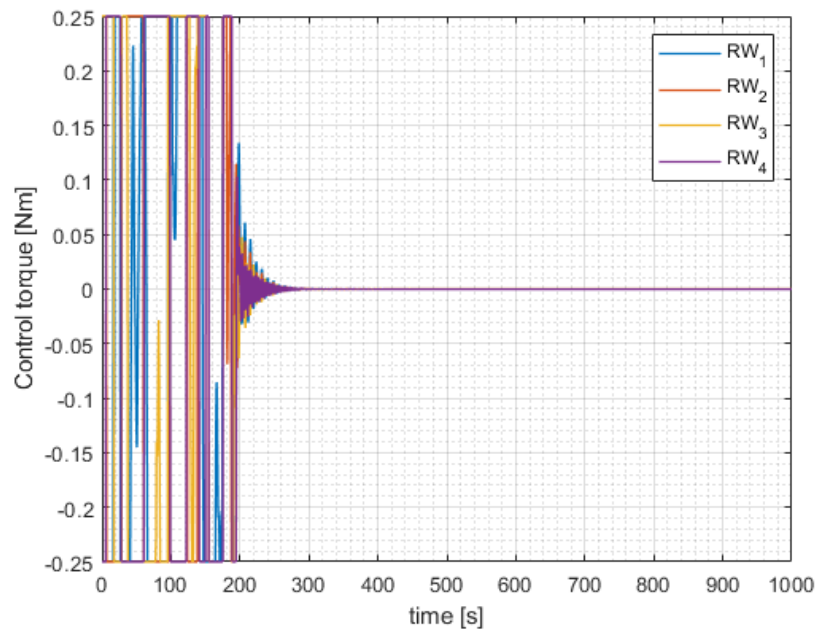


Figure 5.25: Observation phase - Control torques in time

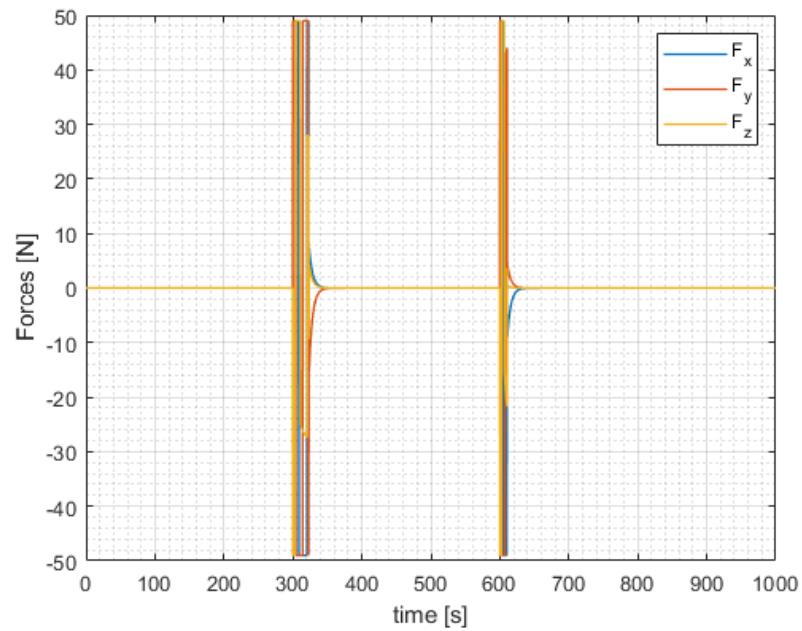


Figure 5.26: Observation phase - Control thrusts in time

## 5.4.2 Capture phase

As previously said in this phase the chaser needs to come closer to the target and capture it with a space manipulator.

The initial condition of this phase are the final of the previous phase, therefore the attitude quaternion is  $\mathbf{q}_{in} = [0.8365, -0.1294, 0.2241, 0.4830]$ , the angular velocities are null, the position vector is  $\mathbf{p}_2 = [-200, 0, 0]$  m and the relative velocities are null.

At the beginning of the simulation, the chaser change again its attitude, coming back to the ideal quaternion. In the meanwhile, after 100 s, another burst is operated in order to arrive to the final position vector  $\mathbf{p}_3 = [-1, 0, 0]$  m with null relative velocities.

Then the target is captured with the space manipulator, becoming a single body with the chaser, causing an increase in the moment of inertia of the chaser. Note that the space manipulator has not been modelled in this work, thus eventual disturbances due to the capture and the manipulator are not considered. Moreover, the chaser's inertia increases by the 40% of its original value.

At  $t = 300$  s the system chaser+target orientate towards the quaternion  $\mathbf{q}_{in}$ , and comes back with a last boost to the position vector  $\mathbf{p}_2$ . When these conditions are reached, the simulation can be considered finished. At this point, in a real scenario, the chaser could bring the target debris into a graveyard orbit or down into the Earth's atmosphere, to burn during the fall.

Figure 5.27 shows the evolution of quaternion error in time. The satellite reaches the ideal quaternion in about 150 s, which is 50 s less than the time needed in the observation phase. This is due to the initial angular velocities, which were not null in the observation phase.

The second attitude manoeuvre lasts about 160 s. Note that at this moment of the simulation the satellite has already captured the target, increasing the moment of inertia, but the time response of the control system does not seem affected by this factor. This shows the robustness of the 1st-SMC.

In figures 5.28 and 5.29 the evolution of position and velocity in time is reported. As can be seen, the first boost is smooth and quick, while the last boost requires a bigger control effort, justified by the control thrusts of figure 5.32.

In figure 5.30 the modal variables in time are reported, while the control torques can be seen in figure 5.31. The vibrations born by the first attitude manoeuvre last for over 200 s, forcing the reaction wheels to work for the first 250 s. The same thing happens during the second attitude manoeuvre, between 300 and 530 seconds from the beginning of the simulation.

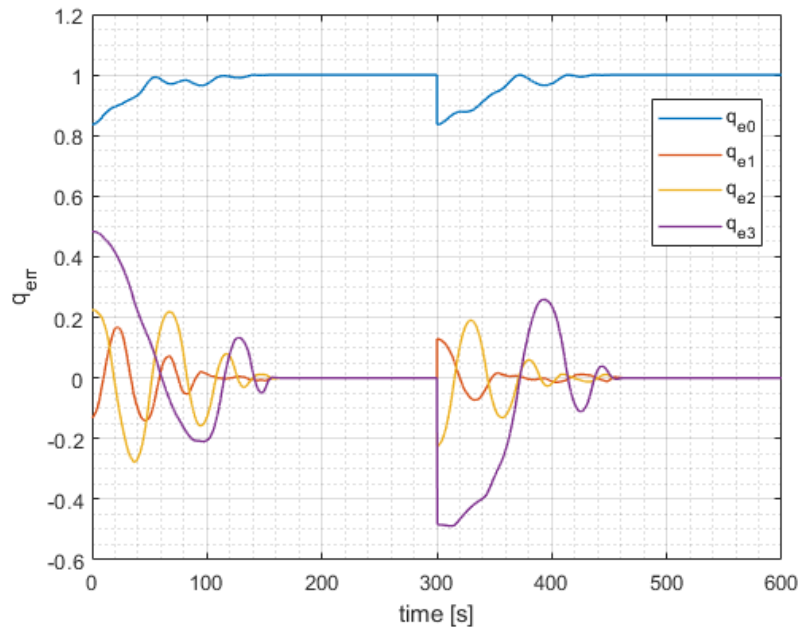


Figure 5.27: Capture phase - Quaternion error in time

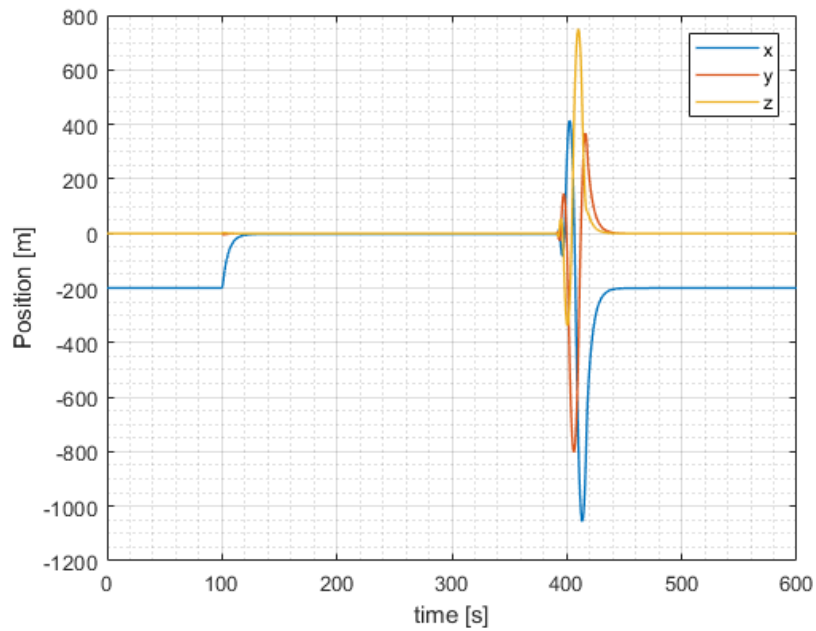


Figure 5.28: Capture phase - Evolution of position in time

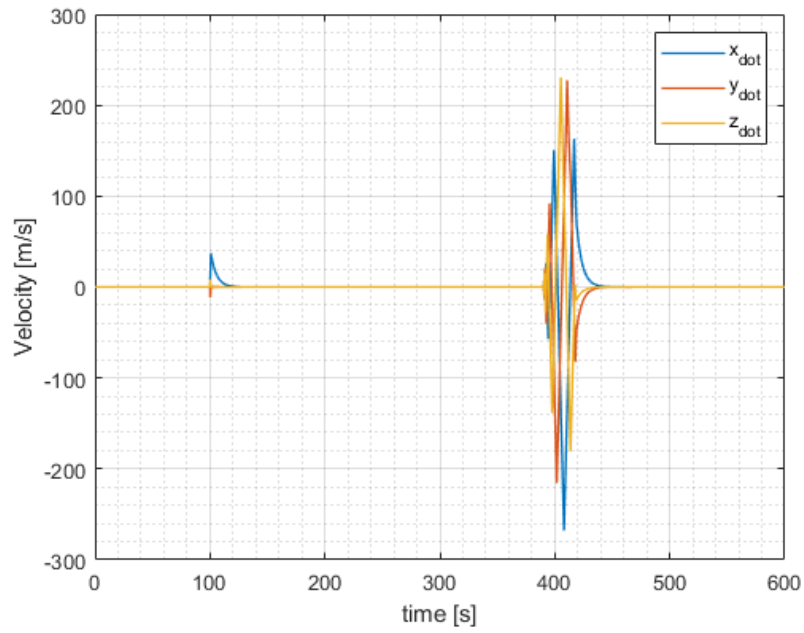


Figure 5.29: Capture phase - Evolution of velocity in time

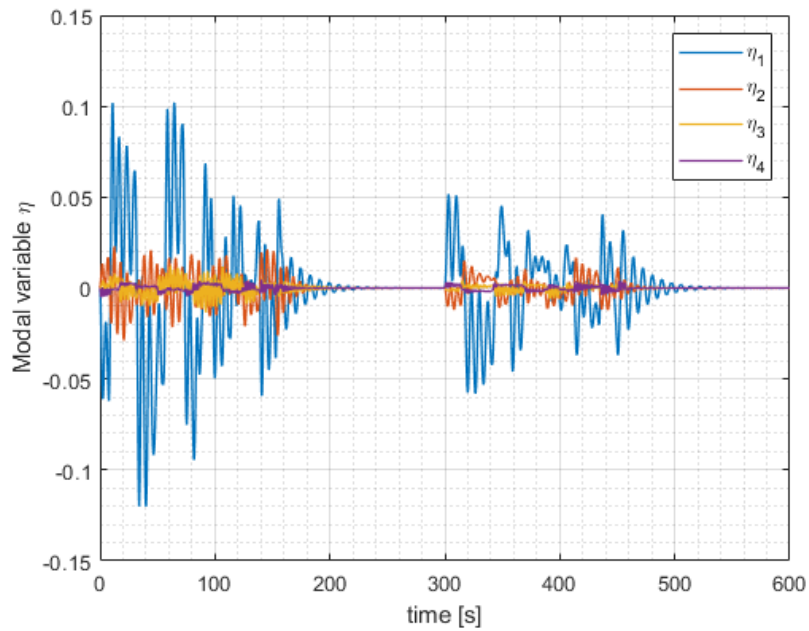


Figure 5.30: Capture phase - Modal variables in time

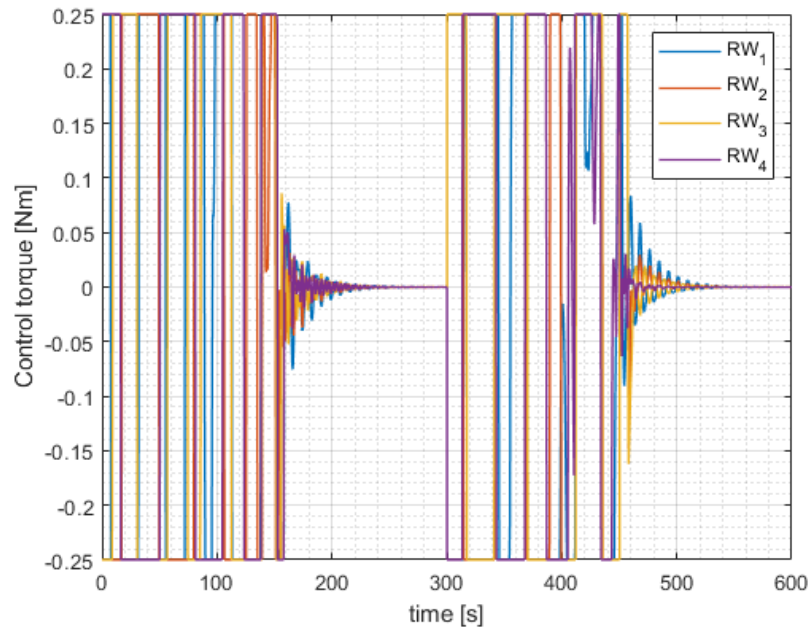


Figure 5.31: Capture phase - Control torques in time

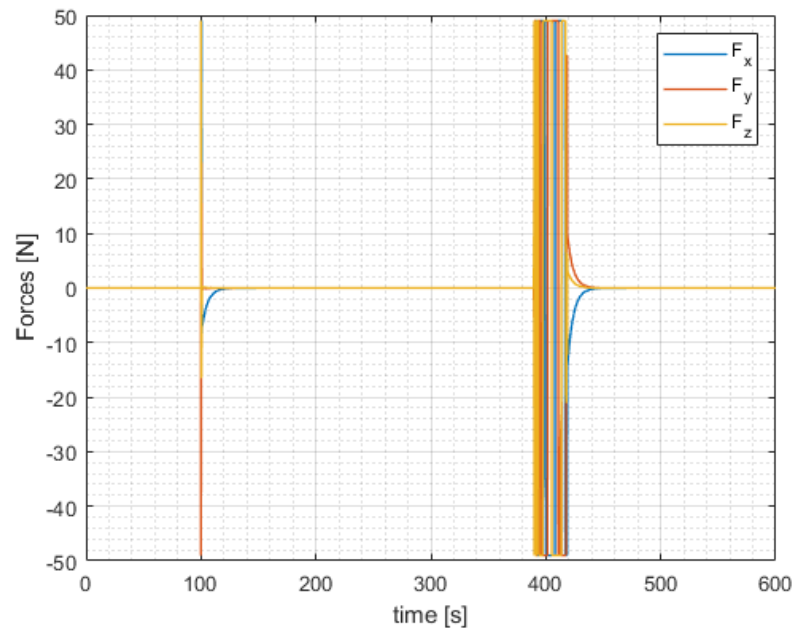


Figure 5.32: Capture phase - Control thrusts in time

## Chapter 6

# Conclusions and Future Works

In the last decades, the market of small satellites has followed a constant growth, due to the reduced launch costs, allowing the non governmental agencies to take part in the space research.

The satellites are often equipped with flexible and deployable appendages (such as space manipulators, solar arrays, antennas, tethers), in order to perform more functions and to occupy a lower volume inside the launcher. But lower masses and volumes cause a higher sensibility to external and internal disturbances. Moreover, the flexible appendages have an important influence on the spacecrafts attitude, due to the coupling between the flexible and rigid components and to the vibrations that could rise during the manoeuvres. Hence, it is crucial to design control techniques robust enough to face these disturbances.

The goal of this thesis was to test the Linear Quadratic Regulator with a non-linear system, and to compare it with two other control laws, both based on the Sliding Mode Control: a First Order SMC and a Continuous Twisting SMC.

In the scenarios seen in Chapter 5, the LQR goes beyond the expectations showing a good robustness against the disturbances due to the flexible components. In fact, it well controls the attitude and position dynamics for the modelled satellite in rest to rest manoeuvre. Instead, it is not able to reach the desired conditions when the satellite has initial angular velocities not null.

Even the Continuous Twisting SMC has not enough control authority for the system proposed in this thesis. It requires control torques too high, not available from the reaction wheels on the market. For this reason, an interesting future work could be the implementation of a propulsion system with the Continuous Twisting SMC, or the implementation of a control moment gyroscope.

The First Order SMC is the only control law that meets the requirements and

constraints presented in this work. It shows great robustness property, facing the external forces, the flexible disturbances and the unknown initial condition. This is why it has been adopted for the Crab Nebula observation mission and the debris capture mission. In both simulations, the desired attitude and position are reached with reasonable settling times, and even the accuracy is great. Hence, considering the satellite modelled in this thesis, the First Order SMC is the best upon the three control laws proposed.

Starting from the work done in this thesis, there are several future works that could be done in order to continue the research.

First, the flexible appendages modelled have been considered with only 1-DoF (Degree of Freedom), it would be interesting to study a case with more DoF, e.g. a space manipulator, and see how it affects the spacecraft's attitude. The reaction torques on the joints of the manipulator, in addition to the vibrations due to the flexible components, could generate very strong disturbances.

Moreover, in the mission presented in Section 5.4, the target debris is captured by the chaser without specifying the system used. The study of the capture system could be another future work, useful to understand the critical issues behind this kind of mission.

At last, it is important to remind that the modelled system has been considered observable and controllable in every moment of the missions, but this is not always true in a real scenario. In addition to this work, some simulations could be run when the state variables are unknown.

# Bibliography

- [1] William Rowan Hamilton, *On quaternions, or on a new system of imaginaries in algebra*, Philosophical Magazine, 1844-1850.
- [2] NASA, *Orbital Debris Quarterly News*, Volume 19-1, January 2015.
- [3] N.L. Johnson, E. Stansbery, D.O. Whitlock, K.J. Abercromby, D. Shoots, *History of On-Orbit Satellite Fragmentation*, 14th edition.
- [4] IADC Scientific and Technical Subcommittee *Space Debris Mitigation Guidelines of the Committee on the Peaceful Uses of Outer Space*.
- [5] Y. Ohkawa, S. Kawamoto, T. Okumura, K. Iki, Y. Horikawa, K. Kawashima, Y. Miura, M. Takai, M. Washiya, O. Kawasaki, D. Tsujita, T. Kasai, H. Uematsu, K. Inoue, *Preparation for an On-Orbit Demonstration of an Electrodynamic Tether on the H-II Transfer Vehicle*, July 31st 2015.
- [6] *e-Deorbit Implementatio Plan*, Clean Space, December 18th 2015.
- [7] D.J. Kessler, N.L. Johnson, J.C. Liou, M. Martney, *The Kessler Syndrome: Implication to Future Space Operations*, 33rd Annual AASGuidance and Control Conference, 2010.
- [8] A.W. Salter, *Space Debris: A Law and Economics Analysis of the Orbital Commons*, 2016.
- [9] Euroconsult, *Prospect for the Small Satellites Market brochure*, 2019, [www.euroconsult-ec.com/research/SS19-brochure.pdf](http://www.euroconsult-ec.com/research/SS19-brochure.pdf) Accessed June 12th 2020.
- [10] T.S. Kelso, *Analysis of Iridium 33 and Cosmos 2251 Collision*, September 2009.
- [11] Crosslink, *Understanding Space Debris: Causes, Mitigation, and Issues*, Vol. 15, No. 1, 2015.
- [12] NASA, *Orbital Debris Quarterly News*, Volume 21-1, February 2017.
- [13] T. Uhlig, F. Sellmaier, M. Schmidhuber, *Spacecraft Operations*, Springer, 2015
- [14] M. Ciarcia, M.E. Grotte, G. Lavezzi, *Attitude Control Strategies for an Imaging Cubesat*, July 2019.
- [15] W. Fehse, *Automated Rendezvous and Docking of Spacecraft*, Cambridge University Press, 2003.
- [16] S. De Gennaro, *Output Stabilization of Flexible Spacecraft with Active Vibration Suppression*, Università di L'Aquila, April 1st 2003.

- [17] M. Mirshams, S. Moradi, A. Ebrahimi, *Design of Deployment Mechanism of Solar Array of a Sample Satellite and Investigation of Deployment on Control Attitude of Satellite*, K.N. Toosy University of Tehran, Iran.
- [18] M. Mancini, E. Capello, E. Punta, *Sliding Mode Control with Chattering Attenuation and Hardware Constraints in Spacecraft Applications*, Politecnico di Torino, Italy.
- [19] M. Mancini, E. Capello, *Robust and Adaptive Attitude Control System for Flexible Reconfigurable Spacecraft*, Politecnico di Torino, Italy, March 31st 2020.
- [20] M. Dentis, E. Capello, *Sliding Mode Techniques for Precise Attitude Control*, 70th International Astronautical Congress, Politecnico di Torino, Italy, October 2019.
- [21] V. Torres-Gonzales, T. Sanchez, L.M. Fridman, J.A. Moreno, *Design of Continuous Twisting Algorithm*, Universidad Nacional Autónoma de México, Mexico, March 28th 2017.
- [22] Blue Canyon Technologies, *Reaction Wheels Data Sheet*, June 2020.
- [23] E. Capello, M. Dentis, *Precise Attitude Control Techniques: Performance Analysis from Classical to Variable Structure Control*, Politecnico di Torino, Italy, September 2019.
- [24] Blue Canyon Technologies, *Reaction Wheels Data Sheet*, June 2020.
- [25] ArianeGroup, *1N, 20N, 400N and Heritage Thruster - Chemical Monopropellant Thruster Family Brochure*, [ww.space-propulsion.com](http://ww.space-propulsion.com) visited on June, 28th, 2020.
- [26] *Copernicus Sentinel-1A satellite hit by space particle*, on [www.esa.int](http://www.esa.int) visited on June 15th 2020.